J. Fluid Mech. (2012), *vol.* 712, *pp.* 471–504. © Cambridge University Press 2012
doi:10.1017/jfm.2012.433

Surface pressure fluctuations on steps immersed in turbulent boundary layers

Minsuk Ji† and Meng Wang

Institute for Flow Physics and Control, Department of Aerospace and Mechanical Engineering, University of Notre Dame, Notre Dame, IN 46556, USA

(Received 18 August 2011; revised 28 August 2012; accepted 29 August 2012; first published online 1 October 2012)

Surface pressure fluctuations induced by turbulent boundary-layer flow at $Re_\theta = 4755$ over small backward- and forward-facing steps are studied with large-eddy simulation. Four step heights that are 53, 13, 3.3 and 0.83 % of the boundary-layer thickness are considered to investigate the effects of step height on surface pressure characteristics and pressure-source mechanisms. The extent to which turbulent velocity fluctuations in the boundary layer and the separated shear layer contribute to the surface pressure fluctuations is examined with scaling of various pressure statistics and two-point correlations. For larger steps, vortical structures develop in the shear layer and the associated intense velocity fluctuations are the dominant source. Downstream of slightly less than one reattachment length from the step, the root-mean-square pressure is found to scale with the local maximum cross-stream Reynolds normal stress $\overline{v'^2}_{max}$. The pressure frequency spectrum at the maximum p_{rms} location consists of an energy-containing range that scales with the mean reattachment length x_r and a higher frequency range that rolls off with a slope close to $-7/3$. As the step height decreases, the boundary-layer turbulent fluctuations become the dominant source, the $\overline{v'^2}_{max}$ scaling of p_{rms} is no longer valid and the roll-off slope of the frequency spectrum becomes steeper. The downstream recovery of a step-perturbed boundary layer towards an equilibrium boundary layer is investigated from the point of view of surface pressure fluctuations. For steps with a strong separated shear layer, pressure fluctuations are found to decay rapidly for up to three reattachment lengths downstream of the step, within which approximately 60 % of the peak p_{rms} is dissipated. Farther downstream, recovery is much slower. The pressure-recovery distances estimated for the largest backward and forward steps are 175 and 295 step heights, respectively.

Key words: hydrodynamic noise, turbulence simulation, turbulent boundary layers

1. Introduction

Turbulent boundary-layer flow over a step surface generates pressure fluctuations larger than those over a smooth surface. The exteriors of road, flight and marine vehicles are commonly found to have small steps and gaps as a result of manufacturing requirements. Although their sizes are typically small – down to a

† Email address for correspondence: minsuk.ji@gmail.com

https://doi.org/10.1017/jfm.2012.433 Published online by Cambridge University Press

few per cent of the boundary-layer thickness, the associated unsteady pressure gives rise to structural vibration, interior noise and noise radiation to the distant field. In order to mitigate these adverse effects and provide required design guidelines, a clear understanding of the nature of surface pressure fluctuations, source mechanisms and their dependence on step height is required.

Pressure fluctuations in subsonic flows over a backward- or forward-facing step have been studied by many researchers (e.g. Mohsen 1968; Fricke 1971; Mabey 1972; Farabee & Casarella 1984, 1986; Efimtsov *et al.* 1999, 2000; Lauchle & Kargus 2000; Lee & Sung 2001, 2002; Brungart *et al.* 2002; Largeau & Moriniere 2007; Camussi *et al.* 2008; Awasthi *et al.* 2011). All these previous studies are experimental and, to our knowledge, there have been no computational studies on pressure fluctuations in step flows. Furthermore, many of them are for large steps whose heights are larger than or comparable to the boundary-layer thickness. Among the studies involving small steps, Farabee & Casarella (1984, 1986) investigated flows over forward and backward steps with step heights approximately 50 % of the boundary-layer thickness and a range of momentum-thickness Reynolds numbers $2600 \leqslant Re_\theta \leqslant 6000$. The maximum root-mean-square (r.m.s.) pressure fluctuations found near the reattachment point of backward and forward steps were 5 and 10 times larger, respectively, than those beneath equilibrium boundary layers. Efimtsov *et al.* (1999, 2000) measured the surface pressure frequency spectra upstream of forward steps and downstream of backward steps at $2800 \leqslant Re_\theta \leqslant 300\,000$ and step heights of approximately 1 to 19 % of the boundary-layer thickness. The spectral level for even the smallest forward step exceeded that of flat-plate boundary layers by more than 20 decibels. In addition, relatively weak dependence of spectra on the Reynolds number was noted. Recently, Awasthi *et al.* (2011) studied flow over forward steps with heights of approximately 60, 15 and 3.8 % of the boundary-layer thickness at two Reynolds numbers $Re_\theta = 15\,500$ and 26 600. Through correlation and spectral analyses, they observed that steps produced disturbance to the boundary-layer pressure spectrum that scaled with the step size. The elevated spectral levels and spatial and temporal scales decayed very slowly with the downstream distance.

Proper scaling relations between the unsteady surface pressure and flow field quantities are not only valuable in engineering design processes, but also helpful in understanding important pressure-producing mechanisms. Early on, Mohsen (1968) suggested that the local maximum Reynolds shear stress $-\rho\overline{u'v'}_{max}$ may be the cause of the large pressure fluctuations. Mabey (1982) noted a strong similarity in the general shape between the streamwise variation of the maximum Reynolds shear stress (Eaton & Johnston 1981) and that of r.m.s. surface pressure fluctuations (Mabey 1972) through the regions of flow separation and reattachment. Subsequently, Simpson, Ghodbane & McGrath (1987) and Na & Moin (1998*b*) showed, using experimental measurements and direct numerical simulations, respectively, that, for separating turbulent boundary layers over a flat plate driven by a strong adverse pressure gradient, the scaling based on the local maximum Reynolds shear stress, rather than the free stream dynamic pressure $\rho U_0^2/2$, resulted in less variation of r.m.s. pressure and better collapse of frequency spectra among different streamwise locations in the separated region. These results led to the belief that the same scaling also applies to the separated flows downstream of steps (Simpson 1989). However, the strength of the shear layer in separated boundary layers above a smooth wall is weaker than that in the step flows. Moreover, all Reynolds stress components, not just the shear component, are indicative of the turbulence strength of the developing shear

https://doi.org/10.1017/jfm.2012.433 Published online by Cambridge University Press

layer, and display a similar variation of the local maximum (e.g. Moss & Baker 1980; Eaton & Johnston 1981).

The extent of the regions with an elevated level of pressure fluctuations downstream of a step is of practical importance. It is related to the boundary-layer relaxation, or recovery to equilibrium conditions following a perturbation. A number of researchers have investigated the boundary-layer recovery process in terms of the flow field, including mean velocities and Reynolds stresses (e.g. Bradshaw & Wong 1972; Alving & Fernholz 1996; Castro & Epik 1998; Song, DeGraaff & Eaton 2000; Tachie, Balachandar & Bergstrom 2001). From the pressure-field point of view, Farabee & Casarella (1984, 1986) observed from the frequency spectra of surface pressure fluctuations that the energized regions of spectra remain identifiable even after 72 and 36 step heights downstream of backward and forward steps, respectively. Awasthi *et al.* (2011) noted that, for their medium step at $Re_\theta = 15\,500$, the disturbance induced by the step was visible in the frequency spectra and the space–time correlations of surface pressure fluctuations even at 150 step heights downstream of the step.

In this paper, we investigate the surface pressure fluctuations on backward and forward steps immersed in an incompressible turbulent boundary layer using large-eddy simulation (LES). The steps are two-dimensional, but the simulations are three-dimensional, with a finite span over which the turbulence is assumed homogeneous. Emphases are on steps that are smaller than the boundary-layer thickness and on the effect of different step heights on the unsteady pressure. The step sizes considered are 53, 13, 3.3 and 0.8 % of the boundary-layer thickness. In experiments, the spatial resolution of pressure measurements is limited by the physical size of the microphone, and may become insufficient for small steps; Efimtsov *et al.* (1999, 2000) thickened the boundary layer considerably with additional screens in order to reduce the step height relative to the boundary-layer thickness while maintaining the step height large enough for measurements. From the simulations, the time history of complete surface pressure data is available along with the flow field data for all steps. Various one-point and two-point pressure statistics are computed and compared among different steps to explain similarities and differences in surface pressure characteristics and important physical processes behind them. Different approaches to scaling of r.m.s. pressure and frequency spectra are assessed. Space–time correlations between fluctuations of surface pressure and velocity in the surrounding region are analysed to understand pressure-source mechanisms. The recovery of perturbed boundary layers downstream of steps is examined in terms of surface pressure fluctuations.

2. Flow configuration and flow fields

LESs of turbulent boundary-layer flows over backward- and forward-facing steps of four different heights were performed by Ji & Wang (2010) to study mechanisms of sound generation. The present study focuses on surface pressure fluctuations and utilizes the validated database obtained from the above simulations. The Reynolds number based on the momentum thickness θ_{st} and the free stream velocity U_0 is $Re_{\theta_{st}} = 4755$. The step heights h are 53, 13, 3.3 and 0.83 % of the boundary-layer thickness δ_{st}. In wall units they are 786, 197, 49 and 12, which places the forward steps in the wake region, upper and lower parts of the logarithmic layer, and the buffer layer of the incoming turbulent boundary layer, respectively. The boundary-layer properties θ_{st} and δ_{st} with the subscript st are measured at the step location in the absence of the step to eliminate dependence on step height. In dimensional units, the largest step height and flow conditions are chosen to match a well-documented case in

https://doi.org/10.1017/jfm.2012.433 Published online by Cambridge University Press

Case	h/δ_{st}	h^+	Re_h
B/F01	0.53	786	25 920
B/F04	0.13	197	6480
B/F16	0.033	49	1620
B/F64	0.0083	12	405

TABLE 1. Flow parameters for different steps. The largest step height is 53 % of the boundary-layer thickness and the subsequent step heights are 1/4 of the preceding one. The upstream boundary layer is identical for all cases and the boundary-layer properties δ_{st} and u_τ are based on an unperturbed turbulent boundary layer at the step location.

the experiment of Farabee & Casarella (1984, 1986): $h = 1.27$ cm and $U_0 = 25$ m s^{-1}. Table 1 summarizes the key dimensionless parameters. For ease of reference in the rest of the paper, the eight simulations are referred to as B01, B04, B16, B64, and F01, F04, F16, F64, where 'B' and 'F' stand for backward and forward steps, respectively, and the largest step corresponds to '01', and the smallest to '64' (1/64 of the largest step).

Details on computational methodology, simulation set-up and validation are described in Ji & Wang (2010). The spatially filtered, incompressible Navier–Stokes equations are solved in conjunction with the dynamic Smagorinsky subgrid-scale model using a second-order finite-difference scheme that is energy-conservative and non-dissipative (You *et al.* 2004). The computational domain size used in the present simulations is $L_x \times L_y \times L_z = 21.3\delta_{st} \times 16.0\delta_{st} \times 2.1\delta_{st}$ for B(F)01, and $10.6\delta_{st} \times 6.4\delta_{st} \times 2.1\delta_{st}$ for the rest of the steps in the streamwise (x), cross-stream (y) and spanwise (z) directions, respectively. With the step vertical face located at $0.5L_x$, the domain lengths downstream of the steps are $20h$, $40h$, $160h$ and $640h$ for B(F)01, B(F)04, B(F)16 and B(F)64, respectively. The grid spacings in wall units are mostly between 8 and 44 in the streamwise direction, between 1.7 and 44 in the cross-stream direction within the boundary layer and approximately 25 in the spanwise direction. The smallest spacings are found adjacent to the step face and the upper and lower surfaces. For the smallest forward step, the grid spacings are halved near the step face in the streamwise and cross-stream directions to provide adequate resolution for the small recirculation bubble upstream of the step. The grid refinement was found to have little effect on the flow statistics downstream of the step face, even though the original grid had only eight points across the step height. This is because the smallest steps, being only 12 wall units high, do not perturb the boundary layer strongly, and the viscous wall unit rather than the number of grid points per step height determines the flow resolution. In the simulations, realistic turbulent inflow is provided at the computational inlet at each time step. The inflow data are generated by a separate LES for a flat-plate boundary layer using the 'rescale and recycle' technique of Lund, Wu & Squires (1998), which ensures not only correct velocity profiles but also correct turbulence structures.

The accuracy of flow quantities obtained by the simulations was verified primarily by considering the largest step simulations B01 and F01, which were chosen to match the experimental conditions of Farabee & Casarella (1984, 1986), and are computationally most demanding. As shown in Ji & Wang (2010), the streamwise distribution of r.m.s. surface pressure fluctuations, pressure frequency spectra at various locations and mean reattachment lengths agree well with the experimental data. The computational domain size and grid resolution were shown to be adequate

https://doi.org/10.1017/jfm.2012.433 Published online by Cambridge University Press

Case	Separation (x_s/h)	Reattachment (x_r/h)
B01	—	5.68
B04	—	5.12
B16	—	7.35
B64	—	8.32
F01	−0.85	2.93
F04	−1.57	2.16
F16	−1.96	—
F64	−1.87	—

TABLE 2. Locations of flow separation upstream of the step and flow reattachment downstream of the step in terms of the step height.

by comparing solutions with those based on different domain sizes and coarser grids. Together with the result of the grid-refinement study for the smallest forward-step case mentioned earlier, this provides sufficient confidence on the grid and domain insensitivity for all the steps considered.

Figure 1 shows the mean streamlines in the vicinity of the step, and table 2 summarizes the mean locations of flow separation (x_s) and reattachment (x_r) as obtained from the zero crossings of the skin friction coefficient (C_f) curve. The coordinate origin is at the step lower corner in the mid-span plane, and the coordinates are normalized with the step height so that, as h decreases, the flow region depicted is closer to the bottom of the boundary layer. For the backward steps, the separation bubble size measured by h changes non-monotonically as the step height is reduced, and the secondary bubble at the step lower corner disappears for B64. For the forward steps, the separation bubble on the step upper surface shrinks as the step height is reduced and eventually disappears for the two smaller steps F16 and F64. The change in bubble size is attributed to varying Re_h (Camussi *et al.* 2008; Awasthi *et al.* 2011). The experimental data of Awasthi *et al.* (2011) indicate the presence of an upper-surface separation bubble for all their steps because of the higher Reynolds number in the experiment. Even though their smallest step matches approximately the F16 case in the present study in terms of h/δ, its Reynolds number, at $Re_h = 5280$, is closer to that for the F04 case, which shows a separation bubble. A recirculation bubble is also present in front of the step lower corner for all step heights. The impingement point on the step face, which characterizes the vertical extent of the front separation bubble, is 0.47, 0.52, 0.61 and $0.55 \times h$, respectively.

The disturbance of a turbulent boundary layer by a step and the resulting flow unsteadiness are closely connected with the surface pressure fluctuations on the step. Varying degrees of flow modification by steps of different heights are illustrated in figures 2 and 3, which display the spatial distribution of turbulent kinetic energy (TKE) and the wall-normal profiles of the streamwise Reynolds normal stress $\overline{u'^2}$, respectively. Increased levels of TKE and $\overline{u'^2}$ are seen for the three larger backward steps, with the maximum occurring along the rear part of the separated shear layer at $x/x_r \simeq 0.75$. On the other hand, flow over the smallest backward step exhibits nearly constant levels since the separated shear layer is too weak to induce much velocity fluctuations. In the case of the forward steps, the two larger ones with a separation bubble on the step upper surface show significantly higher levels of TKE and $\overline{u'^2}$ in the separated shear layer. Interestingly, flow over the second smallest forward step F16 also results in increased levels, although the flow does not separate in the mean

https://doi.org/10.1017/jfm.2012.433 Published online by Cambridge University Press

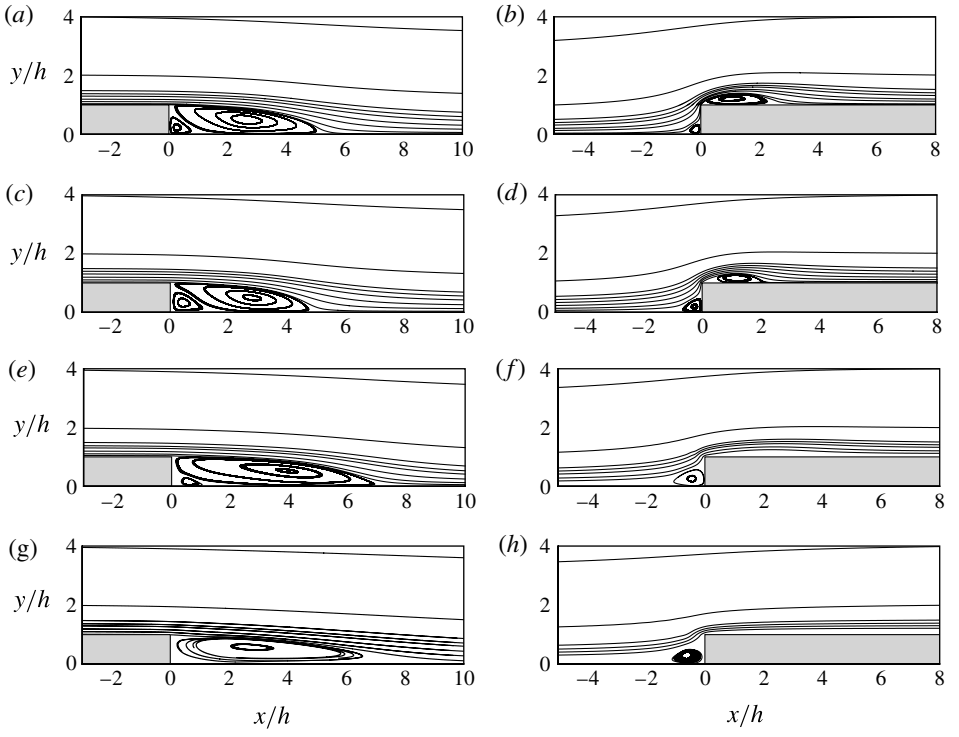


FIGURE 1. Streamlines of the mean flow field around the step for (*a*) B01, (*b*) F01, (*c*) B04, (*d*) F04, (*e*) B16, (*f*) F16, (*g*) B64 and (*h*) F64.

sense and there is no separation bubble. As with B64, the smallest forward step hardly affects the flow downstream of the step. It is pointed out that, for the same step height, the separated shear layers from forward steps are more energetic than those from backward steps, and also that forward steps perturb the outer part of the boundary layer less than backward steps do.

3. Statistics of surface pressure fluctuations

3.1. *Root-mean-square pressure*

Figure 4 shows the streamwise variation of the r.m.s. surface pressure fluctuations normalized by the free stream dynamic pressure $\rho U_0^2/2$. The streamwise coordinate is normalized with different length scales to illustrate how the regions affected by the step change in terms of the step height h (figure 4*a*,*b*), the boundary-layer thickness δ_{st} (figure 4*c*,*d*) and the mean reattachment length x_r (figure 4*e*,*f*). The pressure fluctuations upstream of the backward steps are essentially identical to those of an equilibrium turbulent boundary layer. Following the flow separation at the backward-step upper corner, the p_{rms} drops at the step lower corner, but immediately begins and continues to increase until slightly ahead of the reattachment location ($x/x_r \simeq 0.88$; figure 4*e*), and decreases farther downstream. The magnitudes of the maximum r.m.s. pressure are, from the largest to smallest steps, 5.8, 5.4, 4.4 and 1.6 times that from an equilibrium turbulent boundary layer. Although the step size increases from B64 to B01 by a constant factor of 4, the corresponding increase in the maximum

https://doi.org/10.1017/jfm.2012.433 Published online by Cambridge University Press

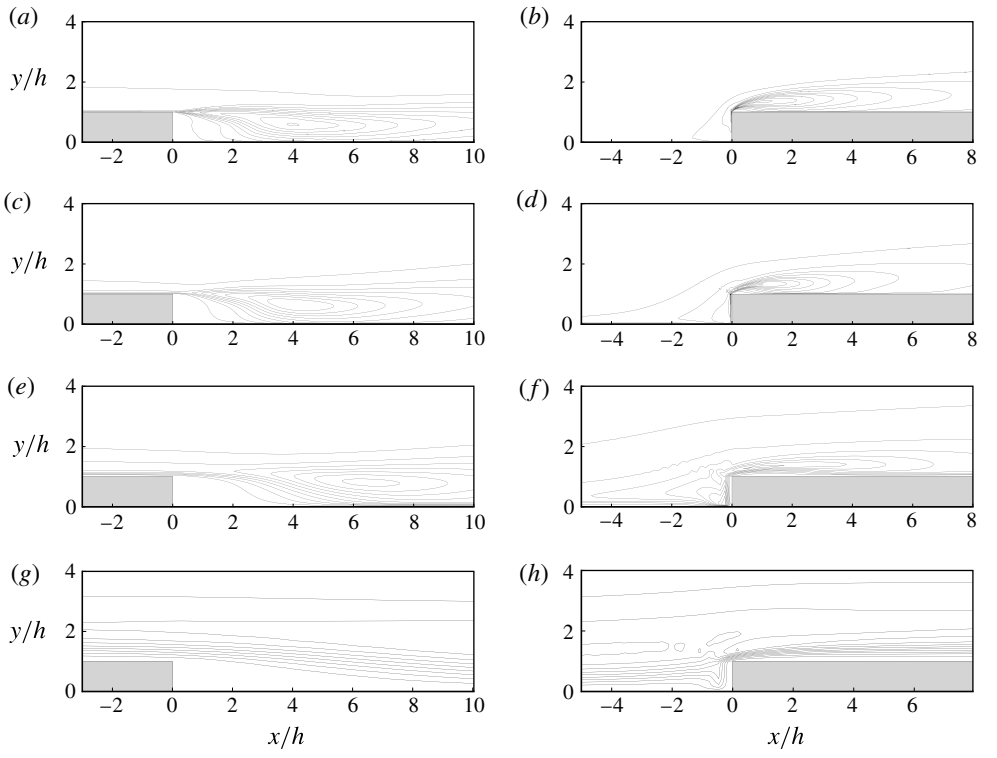


FIGURE 2. Turbulent kinetic energy $(\overline{u'^2}+\overline{v'^2}+\overline{w'^2})/(2U_0^2)$. Eleven contour levels are plotted for: (*a*) B01 from 0.0 to 0.03; (*b*) F01 from 0.0 to 0.1; (*c*) B04 from 0.0 to 0.024; (*d*) F04 from 0.0 to 0.07; (*e*) B16 from 0.0 to 0.014; (*f*) F16 from 0.0 to 0.027; (*g*) B64 from 0.0 to 0.01; and (*h*) F64 from 0.0 to 0.01.

pressure magnitude becomes much smaller with the step height. This 'asymptotic' behaviour of the maximum p_{rms} magnitude will be explained in § 3.4 via analyses of the pressure spectra. The alignment among different backward steps of the maximum p_{rms} location as well as the similarly sloped curves downstream of the maximum shown in figure 4(*e*) suggest that the mean reattachment length is an appropriate length scale for characterizing the surface pressure development downstream of the step as originally proposed by Mabey (1972). Note that Sigurdson (1995) suggested the bubble height as a proper scale for separated flows; for the backward-facing step the bubble height corresponds to the step height and it is the same as the h scaling, which displays more variation among different steps (figure 4*a*).

The maximum p_{rms} of the smallest backward step B64 is much smaller than those of the three larger steps and occurs downstream of the reattachment location at $x/x_r = 1.35$. This implies that different mechanisms for the pressure increase are at work, which is supported by other statistics of the pressure fluctuations in the rest of the paper. Downstream of the pressure peak, the r.m.s. pressure decreases rapidly up to approximately three reattachment lengths, or 15 to 20 step heights behind the step. Farther downstream, it decreases much more slowly. More detailed analyses of the relaxation of pressure fluctuations downstream of steps towards equilibrium boundary-layer values will be described in § 5. Lastly, the normalization based on the

https://doi.org/10.1017/jfm.2012.433 Published online by Cambridge University Press

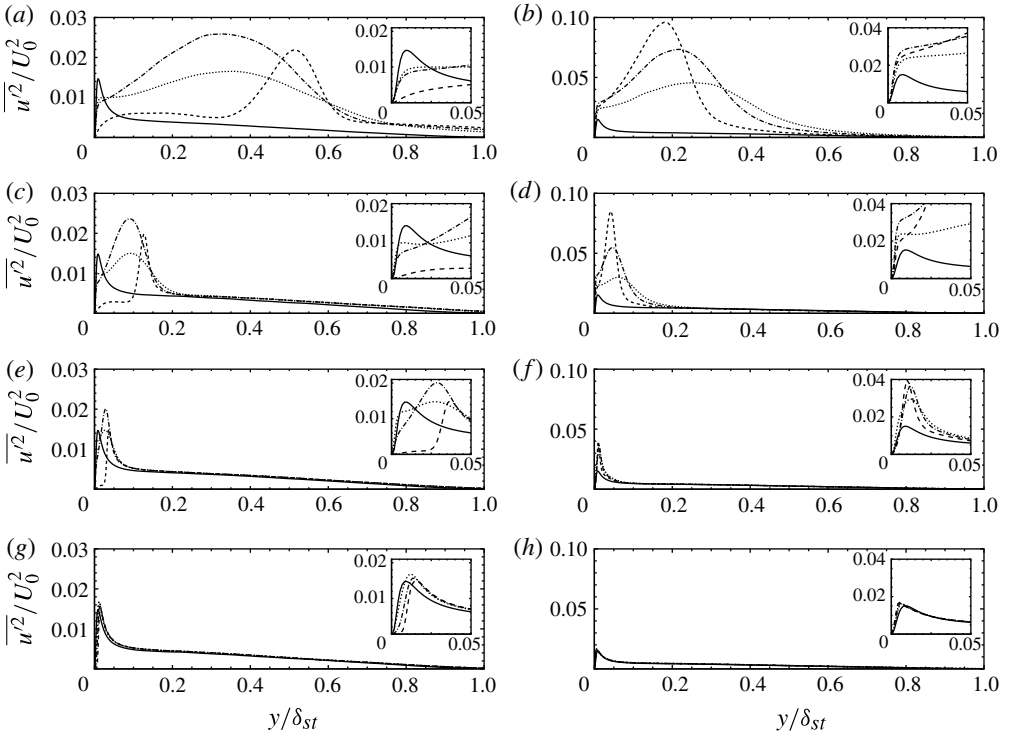


FIGURE 3. Streamwise Reynolds normal stress distribution in cross-stream direction at three downstream locations of (*a*) B01, (*b*) F01, (*c*) B04, (*d*) F04, (*e*) B16, (*f*) F16, (*g*) B64 and (*h*) F64. The figure inset magnifies the near-wall region. Lines for backward steps (left column) are: ——, far-upstream equilibrium boundary layer; – – –, $x/x_r \simeq 0.25$; —·—, $x/x_r \simeq 0.75$; ·····, $x/x_r \simeq 1.5$. Lines for forward steps (right column) are: ——, far-upstream equilibrium boundary layer; – – –, $x/h \simeq 1.0$; —·—, $x/h \simeq 2.2$; ·····, $x/h \simeq 4.0$.

boundary-layer thickness δ_{st} leads to considerably different behaviours among different steps (figure 4*c*).

Forward steps exert greater influence on the upstream pressure fluctuations than do the backward steps because of the adverse pressure gradient and the interaction of the turbulent boundary layer with the step. In terms of the step height (figure 4*b*) p_{rms} begins to increase farther upstream from the step when the step height is smaller, while the opposite is true in terms of the boundary-layer thickness (figure 4*d*). The former observation is consistent with the findings of Efimtsov *et al.* (1999) and Awasthi *et al.* (2011), who observed that the extent of the upstream region with elevated pressure fluctuations does not decrease as fast as the step height. For the flows over the two larger steps F01 and F04, which yield a recirculation bubble downstream of the step, the mean reattachment length is again a good scale, which produces more similar looking p_{rms} curves (figure 4*f*). Their respective maximum r.m.s. pressures, which occur at $x/x_r = 0.60$ and $x/x_r = 0.74$, are much larger than those of backward steps, and 15.4 and 13.7 times the far-upstream boundary-layer value. Flows over the two smaller steps F16 and F64 are without a separation bubble on the step upper surface and the maximum p_{rms} occurs upstream of the step. The pressure fluctuations decrease monotonically downstream of F64, whereas a local maximum is

https://doi.org/10.1017/jfm.2012.433 Published online by Cambridge University Press

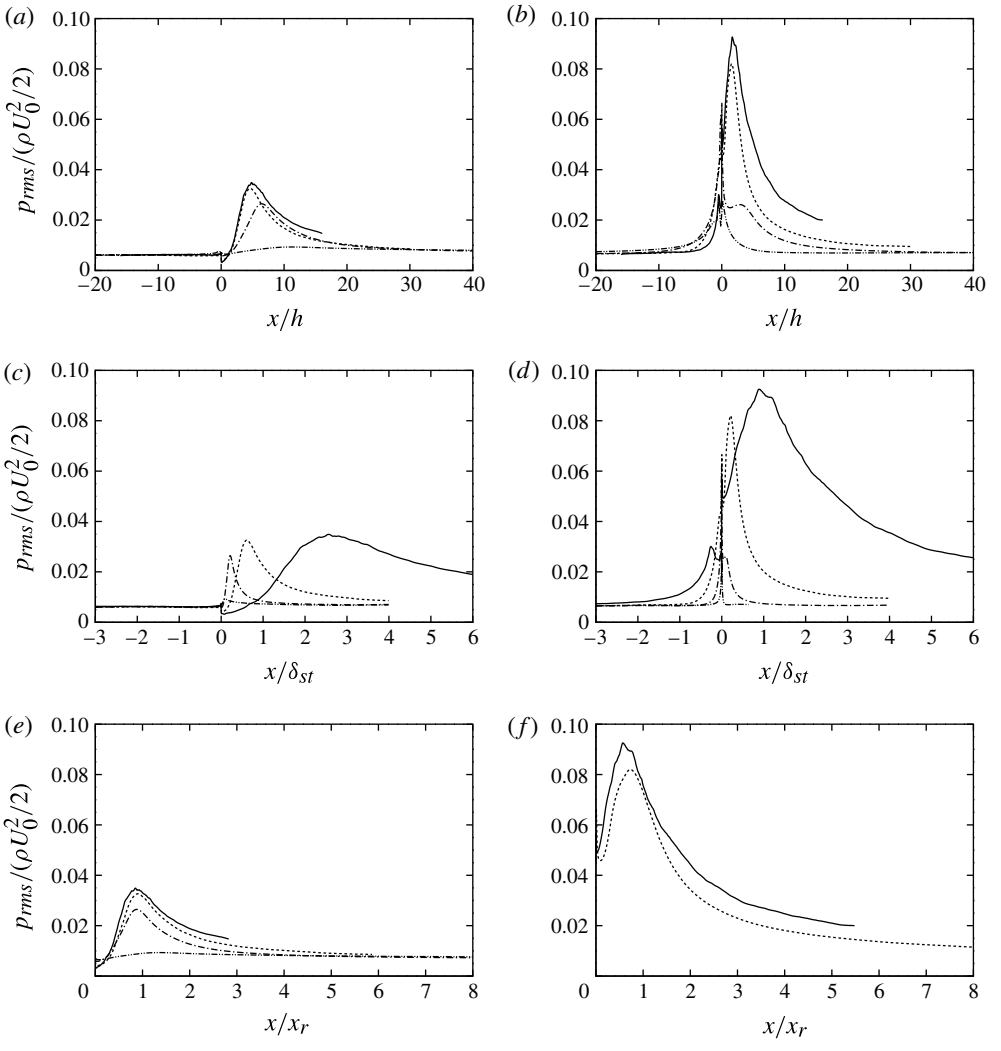


FIGURE 4. Streamwise distribution of r.m.s. fluctuating pressure for (*a*,*c*,*e*) backward-facing step and (*b*,*d*,*f*) forward-facing step. Streamwise coordinate is normalized with (*a*,*b*) h, (*c*,*d*) δ_{st} and (*e*,*f*) x_r. Curves: ——, B(F)01; – – –, B(F)04; — · —, B(F)16; — ·· —, B(F)64.

seen at $x/h = 2.9$ for F16 owing to an increased level of unsteadiness in the shear layer (see figure 2*f*). As with the backward steps, the p_{rms} downstream of the peak first decreases rapidly and then very gradually. For F01, the p_{rms} level at $x/h = 15$, which is near the end of the computational domain, is still significantly higher than that of an equilibrium boundary layer, suggesting a very long recovery distance (see § 5). The r.m.s. pressure for the smallest step F64 quickly recovers to the level of that for an equilibrium boundary layer in less than six step heights downstream of the step.

3.2. *Scaling of the root-mean-square pressure*

Simpson *et al.* (1987) and Na & Moin (1998*b*) used the local maximum Reynolds shear stress $-\rho\overline{u'v'}_{max}$ to scale the p_{rms} and pressure frequency spectra at different streamwise locations in separated turbulent boundary layers. The r.m.s. pressure

https://doi.org/10.1017/jfm.2012.433 Published online by Cambridge University Press

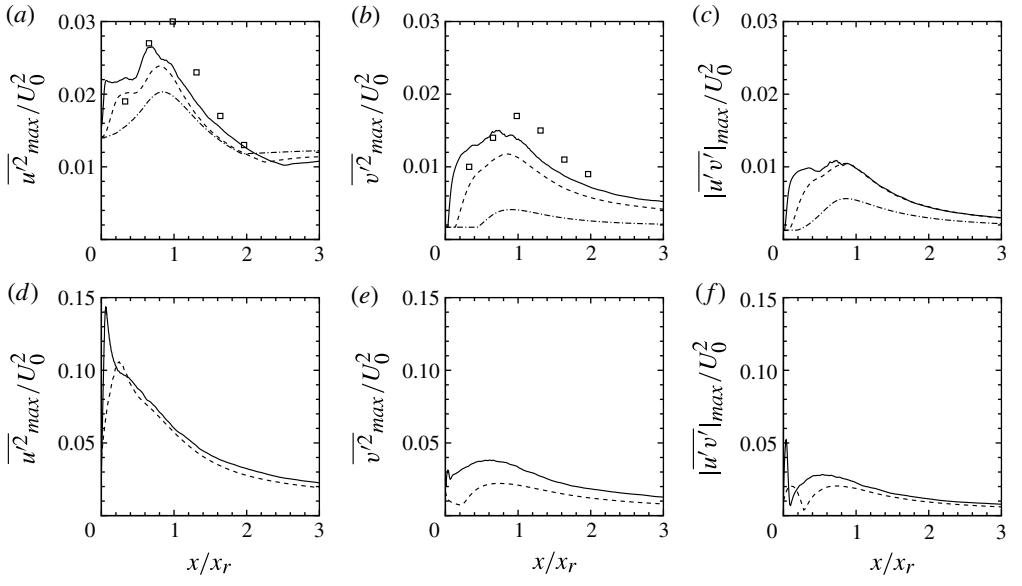


FIGURE 5. Streamwise variation of local maximum of Reynolds stresses downstream of (*a*,*b*,*c*) backward steps and (*d*,*e*,*f*) forward steps. The streamwise coordinate is normalized by the mean reattachment length x_r. Curves: ——, B(F)01; – – –, B(F)04; — · —, B16; □, Chun *et al.* (2004) for a backward step of $h/\delta = 2.03$.

fluctuations showed less variation and the spectra were better collapsed, compared to when the free stream dynamic pressure was used. Simpson *et al.* (1987) hypothesized that the turbulent structures that produce the maximum shear stress in the shear layer influence the surface pressure, and Na & Moin (1998*b*) noted that the vortical structures in the separated shear layer above the separation bubble act as effective source terms for pressure fluctuations. In this section, the premise of the local maximum Reynolds shear stress scaling for surface pressure fluctuations is examined for step flows. Further, the use of other Reynolds stress components, which are also representative of the turbulence in the separated shear layer, is assessed.

The streamwise variation of the local maximum of three Reynolds stress components $\overline{u'^2}$, $\overline{v'^2}$ and $|\overline{u'v'}|$ downstream of the step is shown in figure 5. The streamwise distance is normalized with the mean reattachment length. Because the Reynolds stress scaling investigated here is related to the pressure increase caused by the unsteady separated shear layer, the two smaller forward steps F16 and F64 without a downstream separation bubble and the smallest backward step B64 with a weak shear layer are excluded from consideration. For the backward steps, all three Reynolds stress components increase in magnitude following the separation, obtain a peak slightly upstream of the reattachment location, and decrease from there on. Note that the abrupt change in the slope of the $\overline{u'^2}_{max}$ curves at $2 \leqslant x/x_r \leqslant 2.5$ (figure 5*a*) is caused by the shift in location of the maximum stress from the shear layer to the near-wall region, as the shear layer weakens and the near-wall turbulent structures redevelop (see figure 3). Also shown in the figure are the experimental data of Chun, Liu & Sung (2004) for flow over a backward-facing step with $Re_h = 33\,000$ and $h/\delta = 2.03$ ($\overline{u'v'}$ component is not available). The trend is similar to that of the computational results, but the magnitudes of the peaks are slightly larger because

https://doi.org/10.1017/jfm.2012.433 Published online by Cambridge University Press

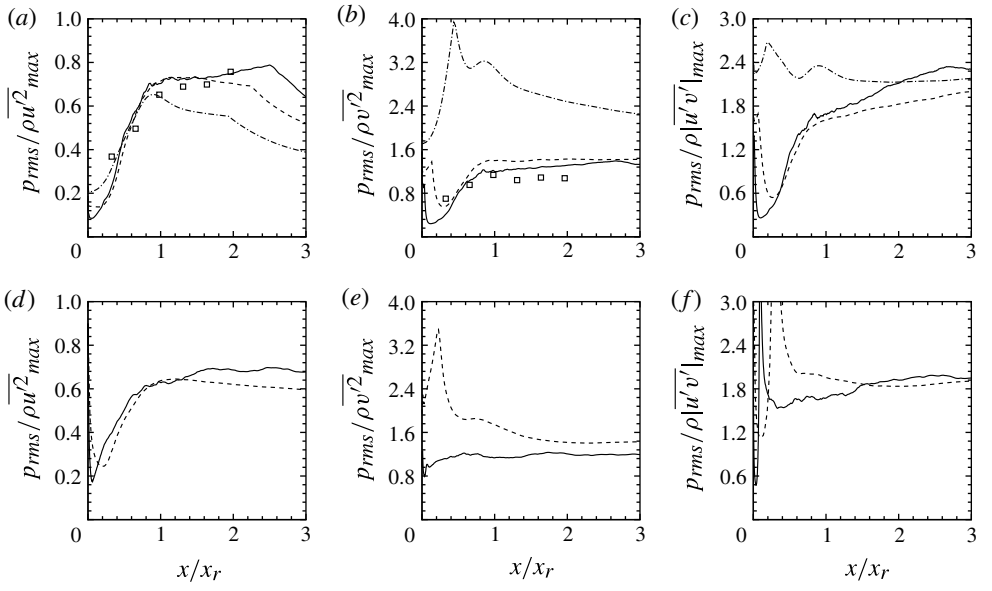


FIGURE 6. Streamwise variation of r.m.s. pressure fluctuations scaled with different Reynolds stress components of figure 5: (*a*,*b*,*c*) backward steps and (*d*,*e*,*f*) forward steps. The streamwise coordinate is normalized by the mean reattachment length x_r. Curves: ——, B(F)01; – – –, B(F)04; — · —, B16; □, Chun *et al.* (2004) for a backward step of $h/\delta = 2.03$.

of the larger ratio of step size to boundary-layer thickness. For the forward steps, $\overline{u'^2}_{max}$ attains a maximum at a small distance behind the step corner and decreases farther downstream, while $\overline{v'^2}_{max}$ and $|\overline{u'v'}|_{max}$ increase up to approximately 60 % of the reattachment length and decrease farther downstream. Near the forward-step corner, positive Reynolds shear stresses are observed.

Figure 6 presents the p_{rms} scaled by the local maximum Reynolds stresses shown in figure 5. When the streamwise normal stress $\rho\overline{u'^2}_{max}$ is used (figure 6*a*,*d*), the curves for all backward steps collapse between $0.4x_r$ and $0.8x_r$. Similarly, the curves for forward steps show reasonable collapse between $0.4x_r$ and $1.2x_r$. The collapsed curves, however, show a streamwise variation. When the cross-stream normal stress $\rho\overline{v'^2}_{max}$ is used (figure 6*b*,*e*), the p_{rms} from B01 and B04 coincide for $x/x_r \geqslant 0.4$, while that from B16 differs significantly. This can be explained by figure 5(*b*), which shows that the growth of $\overline{v'^2}_{max}$ downstream of B16 is much delayed, and its peak magnitude is smaller. For the forward steps, the p_{rms} for F04 differs significantly from that of F01 in the front part of the separated region, but they approach each other farther downstream. For both backward and forward steps, a smaller step height results in larger values of $p_{rms}/\rho\overline{v'^2}_{max}$ but, as the step height increases, the normalized p_{rms} approaches approximately 1.35 in the rear part of the recirculation bubble and farther downstream. The values calculated from the experimental data of Chun *et al.* (2004) agree reasonably well with the simulation results for B01 and B04 although their step height is twice the boundary-layer thickness, suggesting that the result is insensitive to the step height once it exceeds a threshold value. When the Reynolds shear stress $\rho|\overline{u'v'}|_{max}$ is used (figure 6*c*,*f*), the p_{rms} for B01 and B04 coincide in the

https://doi.org/10.1017/jfm.2012.433 Published online by Cambridge University Press

rear part of the recirculation region while all curves converge to approximately 2.15 for $x/x_r \gtrsim 2$. For the forward steps, the p_{rms} for F01 and F04 differ in the front part of the separated region, but converge to approximately 1.9 farther downstream. The large oscillations near the forward-step corner are due to the sign change of $\overline{u'v'}_{max}$. In the previous studies on separated boundary layers, the observed maximum Reynolds shear stresses $-\overline{u'v'}/U_0^2$ were 0.0017 (Na & Moin 1998*a*,*b*) and 0.006 (Simpson, Chew & Shivaprasad 1981; Simpson *et al.* 1987), which are closest to that from B16. In the separated flow region, the r.m.s. pressure scaled by $\rho|\overline{u'v'}|_{max}$ varied from 2.4 to 3.1 for the former and from 3.6 to 4.4 for the latter. It is interesting to observe that, for B16, it changes from 2.2 to 2.7 inside of the separation bubble.

The above observations can be summarized as follows. The streamwise Reynolds normal stress scaling yields the best collapse of the p_{rms} in the separated region among steps of different heights. However, the scaled r.m.s. pressure is not constant and increases almost linearly with downstream distance. When $\rho\overline{v'^2}_{max}$ is used, the r.m.s. pressure for larger steps (B01, B04, and F01, F04) approaches 1.35 in the rear part of the recirculation bubble and remains constant with downstream distance. Therefore, the cross-stream Reynolds normal stress $\rho\overline{v'^2}_{max}$ appears to be the best scale for the fluctuating surface pressure for steps that are sufficiently large to generate a strong separated shear layer. For equilibrium flat-plate boundary layers, it is known that the vertical velocity component is most closely related to the surface pressure fluctuations (Kraichnan 1956; Panton & Linebarger 1974). The current results indicate that the same is true for the highly non-equilibrium flows less than one reattachment length downstream of backward and forward steps. The scaling based on the Reynolds shear stress $\rho|\overline{u'v'}|_{max}$, although somewhat satisfactory, performs worse than $\rho\overline{v'^2}_{max}$ and shows a difference between backward and forward steps.

3.3. *Frequency spectra*

The frequency spectra of pressure fluctuations on the backward steps at four streamwise locations are shown against the non-dimensional frequency $f\delta_{st}/U_0$ in figure 7. It depicts changes in the spectral level and shape at different streamwise locations. For reference, the frequency spectrum for the far-upstream equilibrium boundary layer is plotted as a dotted line. Upstream of the steps, the spectra are similar to that of the unperturbed boundary layer until the flow is very close to the step upper corner. At $x \simeq -0.3h$ (figure 7*a*), an increased energy level is observed mostly in the low-frequency range, possibly due to edge diffraction, while the high-frequency part of the spectrum is unchanged. Note that, owing to non-uniform streamwise grid spacing, which is minimum at the step face, the high-frequency spectral content is better resolved near the step face and the spectrum of the far-upstream boundary layer falls off faster at high frequencies. For an equilibrium boundary layer, the difference between the p_{rms} computed on the coarser, upstream grid and that on the finer, near-step grid is less than 5 %. Close to the step lower corner inside of the separation bubble ($x \simeq 0.05x_r$; figure 7*b*), the low-frequency part of the spectrum is similar to that of the upstream spectrum shown in figure 7(*a*), whereas the high-frequency portion is strongly dependent on the step height. Larger steps see a larger decrease in high-frequency energy level because the small eddies in the separated flow are farther away from the step lower surface. This also explains the drop in the p_{rms} immediately downstream of the two largest steps (see figure 4). Farther downstream inside of the recirculation bubble (figure 7*c*,*d*), the spectral level increases at all frequencies for all steps except the smallest as the turbulence level increases in the separated shear layer and the shear layer moves closer to the wall. The

https://doi.org/10.1017/jfm.2012.433 Published online by Cambridge University Press

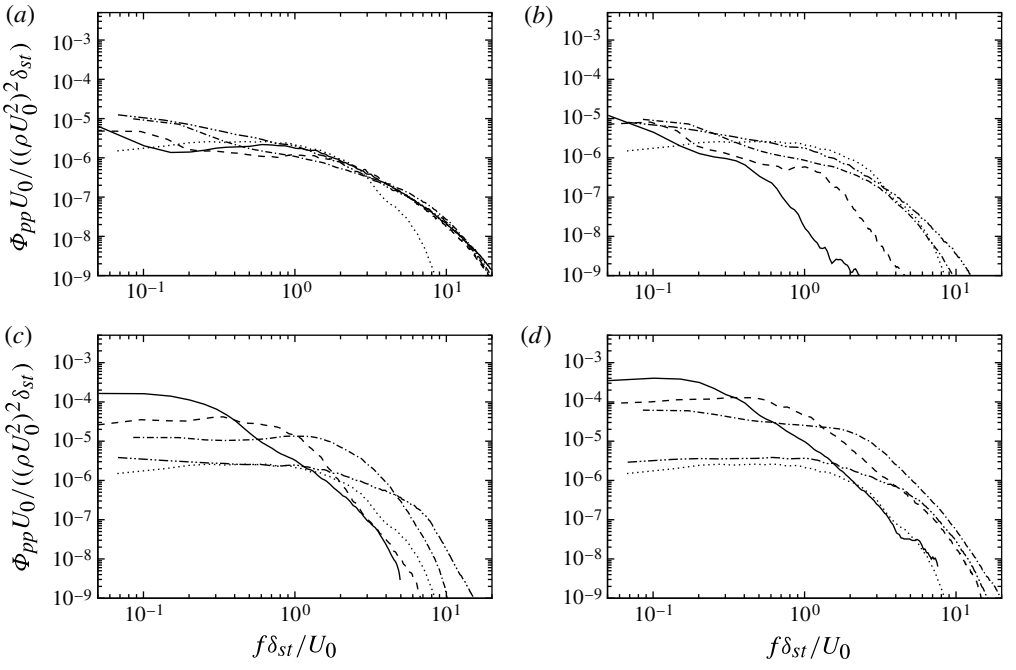


FIGURE 7. Frequency spectra of fluctuating surface pressure for backward-facing steps at four streamwise locations: (*a*) $x \simeq -0.3h$; (*b*) $x \simeq 0.05x_r$; (*c*) $x \simeq 0.5x_r$; and (*d*) $x \simeq x_r$. Curves: ——, B01; – – –, B04; — · —, B16; — ·· —, B64; · · · · · ·, far-upstream equilibrium boundary layer.

spectral level for the smallest step B64 decreases at lower frequencies while increasing slightly at higher frequencies.

Plotted in figure 8 are the frequency spectra for the forward steps. Since not all forward steps induce a separation bubble on the upper surface, the spectra are plotted at the same locations measured in h instead of x_r. At $x \simeq -6h$ (figure 8*a*), the spectral level already experiences an increase in the low-frequency range. The increase is larger for smaller steps in accordance with the earlier observation of p_{rms} and experimental results of Efimtsov *et al.* (1999) and Awasthi *et al.* (2011). At $x \simeq -h$ (figure 8*b*), the spectral levels are significantly raised from that of the far-upstream boundary layer; even the smallest step experiences a two-decade increase at low frequencies. All steps except the largest display similarly elevated pressure spectra, while the spectrum from the largest step lacks in mid- to high-frequency content. This is due to the lift-up of the boundary layer close to the step. As the step size decreases, the recirculation bubble in front of the step becomes larger in terms of the step height (see figure 1), but smaller in terms of a common length scale such as δ_{st}. Therefore, the boundary layer, which is shifted upward of the recirculation bubble, is farthest from the step lower surface for the largest step and results in lower energy level at higher frequencies. Figure 8(*c*) shows the frequency spectra at $x \simeq h$. For the two larger steps, this location is inside of the recirculation bubble (33 and 50 % of the respective bubble sizes of F01 and F04) and the increase in the spectral level is caused by the enhanced turbulence in the separated shear layer. On the other hand, the spectral level is decreased for the two smaller steps F16 and F64, which do not produce a separation

https://doi.org/10.1017/jfm.2012.433 Published online by Cambridge University Press

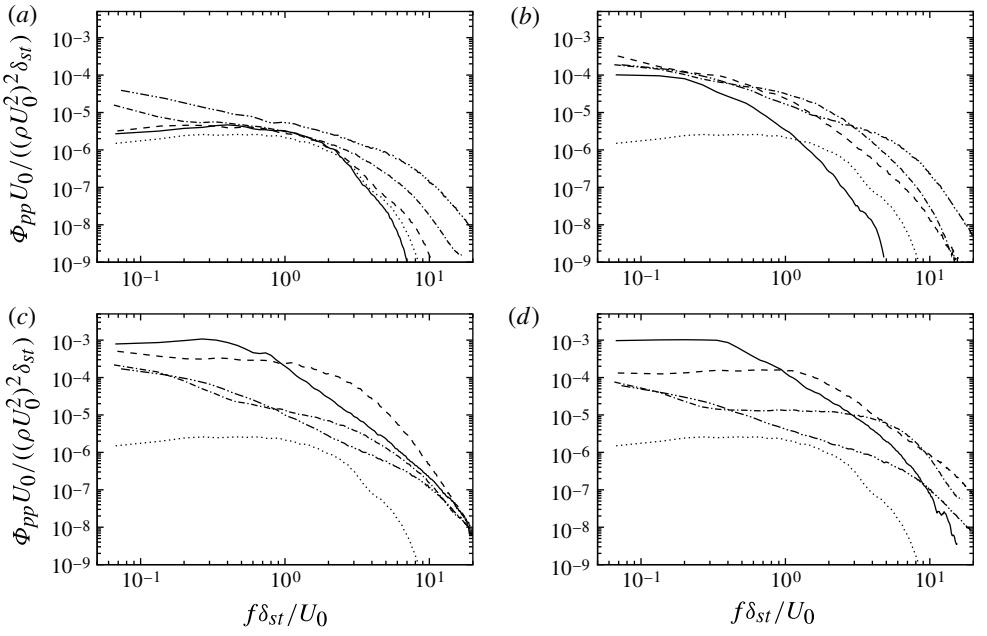


FIGURE 8. Frequency spectra of fluctuating surface pressure for forward-facing steps at four streamwise locations: (*a*) $x \simeq -6h$; (*b*) $x \simeq -h$; (*c*) $x \simeq h$; and (*d*) $x \simeq 3h$. Curves: ——, F01; – – –, F04; — · —, F16; — ·· —, F64; · · · · · ·, far-upstream equilibrium boundary layer.

bubble downstream of the step. At $x \simeq 3h$, the spectral level is decreased for all steps except for F01, whose reattachment location is just upstream of this location. The development of surface pressure frequency spectra farther downstream of the backward and forward steps is discussed in § 5 in the context of boundary-layer recovery to equilibrium conditions.

It should be noted that, in the previous figures as well as those in the rest of the paper, different length scales are used to present results. Step height h and boundary-layer thickness δ_{st} are two independent length scales that are both important, and the reattachment length x_r is another relevant length scale when there is separation. In each figure the most appropriate length scale is used to best illustrate the flow physics or provide the best scaling. The reattachment length x_r generally provides the best scaling for the unsteady wall-pressure statistics, but it is not applicable for the two smallest forward steps, which produce no downstream separation, and therefore the step height h is sometimes used instead to present results for all four forward steps. When separation is present, it may appear that h and x_r are interchangeable because the flow structures scale with both. However, h cannot differentiate the flow effect; for example, F01 and B01 are of the same height, but their recirculation bubble sizes, and thus the flow structures, are quite different.

3.4. *Scaling of the frequency spectra*

Figure 9 shows the pressure spectra normalized with the mean reattachment length and twice the free stream dynamic pressure at the streamwise location of maximum p_{rms}. Those from the two smaller forward steps F16 and F64 and the smallest backward step B64 are not shown because the lack of the step downstream separation bubble and the weak shear layer make the pressure statistics qualitatively different (see figures 4, 7*d*

https://doi.org/10.1017/jfm.2012.433 Published online by Cambridge University Press

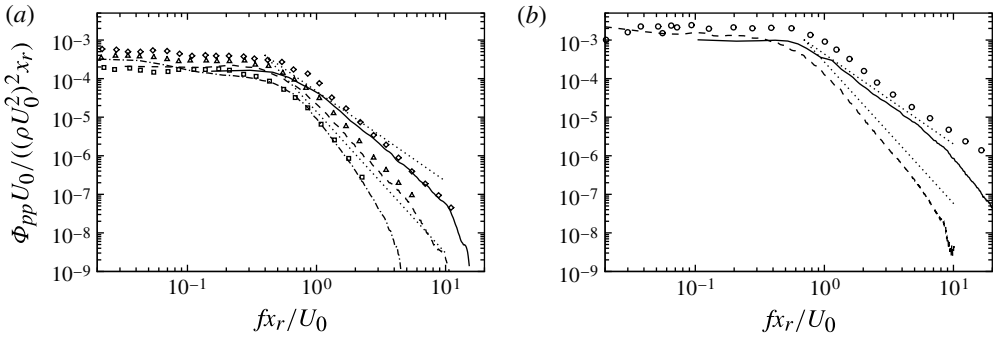


FIGURE 9. Frequency spectra of fluctuating surface pressure scaled with the mean reattachment length x_r at the maximum p_{rms} location of (*a*) backward steps and (*b*) forward steps. Curves: ——, B(F)01; – – –, B(F)04; — · —, B16. The two dotted straight lines have slopes $-7/3$ (upper) and $-11/3$ (lower). Symbols are experimental data: (*a*) Efimtsov *et al.* (2000) for $h/\delta \simeq 19.3\,\%$ (◇), $9.7\,\%$ (△) and $3.9\,\%$ (□); (*b*) Awasthi *et al.* (2011) for $h/\delta \simeq 60\,\%$ (○).

and 8*d*). Also plotted in figure 9 are the experimental data of Efimtsov *et al.* (2000) and Awasthi *et al.* (2011). The spectral level begins to roll off at $fx_r/U_0 \simeq 0.6$ for both backward and forward steps. This frequency, often referred to as the 'vortex-shedding' frequency in the literature, agrees with those from previous studies of separated and reattaching flows; see, for instance, table 1 in Dandois, Garnier & Sagaut (2007).

With the x_r scaling, the spectral levels of the energy-containing scales ($fx_r/U_0 \leqslant 0.6$) display much less variation among B01, B04 and B16 (compare figures 7*d* and 9*a*) and between F01 and F04 (compare figures 8*d* and 9*b*) than when δ_{st} is used. The experimental data exhibit similar spectral levels for $fx_r/U_0 \leqslant 0.6$ as the computation results but show a wider spread, possibly because of the wide range of Re_θ in the experiment. Therefore, it is suggested that the large-scale, low-frequency pressure fluctuations are generated by flow structures of size comparable to x_r (also see figure 16).

In the frequency range $fx_r/U_0 > 0.6$, both the simulation and experimental data display dependence of spectral roll-off rate on step height. The slope becomes less steep for larger step heights, and those from B01 and F01 are close to $-7/3$. In the literature, slopes of $-7/3$ (Lee & Sung 2001; Camussi, Guj & Ragni 2006) and $-5/2$ (Leclercq *et al.* 2001; Awasthi *et al.* 2011) have both been cited, which are very close. In consideration of turbulent free-shear flows, where turbulence–turbulence interaction leads to $-7/3$ slope in the pressure spectrum and turbulence–mean shear interaction results in $-11/3$ slope (George, Beuther & Arndt 1984), it is suggested that the effect of turbulence–turbulence interaction becomes more prominent as the step height increases. The increase in turbulent kinetic energy levels (figure 2) as well as the convergence of the Reynolds-stress-scaled p_{rms} with increasing step height (figure 6*b*,*e*) support this.

It was observed in § 3.1 that the incremental increase in the maximum $p_{rms}/(\rho U_0^2/2)$ becomes smaller as the step height increases. The two features of the pressure spectrum noted above – collapse of the spectra for $fx_r/U_0 \leqslant 0.6$ and the step-height-dependent slope for $fx_r/U_0 > 0.6$ – help to explain this. Steps of a height that is sufficiently large compared to the boundary-layer thickness allow the separated shear layer to develop sufficiently, and will have similar spectral levels for $fx_r/U_0 \leqslant 0.6$ and similar roll-off slopes of $-7/3$ for $fx_r/U_0 > 0.6$. Consequently, they will have nearly

https://doi.org/10.1017/jfm.2012.433 Published online by Cambridge University Press

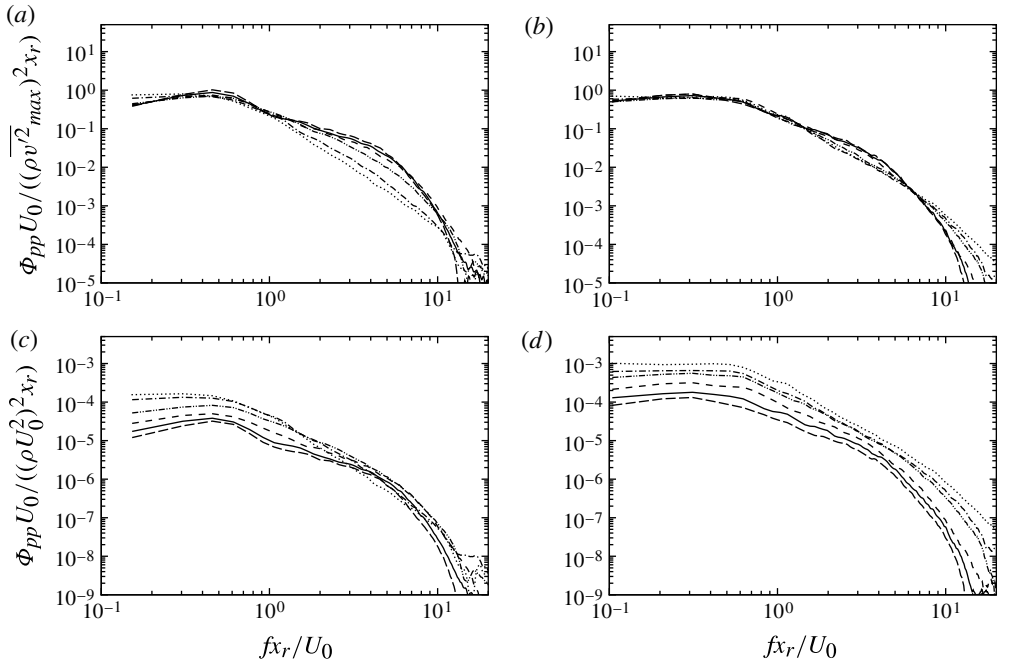


FIGURE 10. Frequency spectra of fluctuating surface pressure scaled in two different ways for (*a*,*c*) B01 and (*b*,*d*) F01. For B01, x/x_r (x/h) values are: ·····, 0.88 (5.02); —·—, 1.02 (5.77); —··—, 1.32 (7.50); – – –, 1.76 (10.0); ——, 2.2 (12.5); — —, 2.64 (15.02). For F01, x/x_r (x/h) values are: ·····, 0.6 (1.75); —·—, 1.02 (2.99); —··—, 1.2 (3.51); – – –, 1.79 (5.24); ——, 2.4 (7.02); — —, 3.0 (8.75).

the same magnitude of $p_{rms}/(\rho U_0^2/2)$ (proportional to the area under the spectrum in figure 9), provided the flow configuration is the same, i.e. backward or forward step. In fact, from the literature, the peak p_{rms} from subsonic flows over backward steps of many different heights is approximately 4 % of the dynamic pressure, and that from forward steps is approximately 10 % (e.g. Mohsen 1968; Mabey 1972; Lee & Sung 2001; Camussi *et al.* 2008).

Figure 10 compares the pressure spectra scaled by the local maximum cross-stream Reynolds normal stress $\rho\overline{v'^2}_{max}$ with those scaled by twice the dynamic pressure for the cases of the largest steps B01 and F01 at different streamwise locations starting from the rear part of the separation bubble. Consistent with the p_{rms} scaling (cf. figures 4 and 6), the spectra at different locations collapse well when $\rho\overline{v'^2}_{max}$ is used, but do not collapse when scaled by the dynamic pressure. As observed in figure 6, $p_{rms}/\rho\overline{v'^2}_{max}$ is nearly invariant with x at these locations. Figure 10 further demonstrates that not only the magnitude but also the frequency distribution of the fluctuation surface pressure are nearly invariant with x downstream of the rear part of the separation bubble. The small rise in the normalized pressure spectra with x for B01 in the mid- to high-frequency range, as seen in figure 10(*a*), is responsible for the slight increase in $p_{rms}/\rho\overline{v'^2}_{max}$ with x observed in figure 6(*b*).

3.5. *Space–time correlations*

One-point pressure statistics and its scalings provided indirect evidence of different pressure-inducing mechanisms for steps of different heights. Two-point statistics

https://doi.org/10.1017/jfm.2012.433 Published online by Cambridge University Press

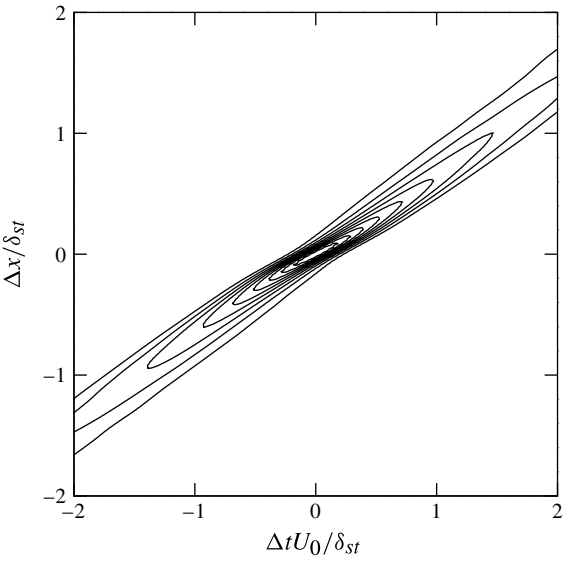


FIGURE 11. Space–time correlation coefficient $C_{pp}(\Delta x, \Delta t; x)$ upstream of B64 at $x = -2.5\delta_{st}$. Contour levels are from 0.1 to 0.9 with increments of 0.1.

is a more direct means for understanding such mechanisms because it allows identification of flow structures that are responsible for pressure fluctuations. This section examines the space–time correlations of surface pressure, and § 4 will investigate the pressure–velocity correlations.

The space–time correlation of surface pressure fluctuations is defined as

$$R_{pp}(\Delta \boldsymbol{x}, \Delta t; \boldsymbol{x}) = \langle p'(\boldsymbol{x}, t) p'(\boldsymbol{x} + \Delta \boldsymbol{x}, t + \Delta t) \rangle, \tag{3.1}$$

where the angle brackets denote averaging in time and the homogeneous spanwise direction. The corresponding correlation coefficient is

$$C_{pp}(\Delta \boldsymbol{x}, \Delta t; \boldsymbol{x}) = \frac{R_{pp}(\Delta \boldsymbol{x}, \Delta t; \boldsymbol{x})}{R_{pp}\,(0, 0; \boldsymbol{x})^{1/2}\, R_{pp}\,(0, 0; \boldsymbol{x} + \Delta \boldsymbol{x})^{1/2}}. \tag{3.2}$$

As a reference, figure 11 depicts contours of the correlation coefficient as a function of streamwise spatial and temporal separations at $-2.5\delta_{st}$ upstream of B64; it is representative of an equilibrium boundary layer. The convection velocity of surface pressure fluctuations can be defined as the ratio $\Delta x/\Delta t$ that maximizes $C_{pp}(\Delta x, \Delta t)$, and loosely interpreted as the slope of the slender closed contours in figure 11. The convection velocity associated with a specific frequency ω can be calculated from the cross-spectrum of pressure fluctuations

$$\Phi_{pp}(\Delta x, \omega; x) = \frac{1}{2\pi} \int_{-\infty}^{\infty} R_{pp}(\Delta x, \Delta t; x) \mathrm{e}^{\mathrm{i}\omega \Delta t}\, \mathrm{d}(\Delta t), \tag{3.3}$$

since its phase angle ϕ is related to the convection velocity $U_c(\Delta x, \omega; x)$ via (see e.g. Bendat & Piersol 2000)

$$\frac{\omega \Delta x}{U_c(\Delta x, \omega; x)} = \phi(\Delta x, \omega; x) = \tan^{-1} \frac{\mathrm{Im}\{\Phi_{pp}(\Delta x, \omega; x)\}}{\mathrm{Re}\{\Phi_{pp}(\Delta x, \omega; x)\}}, \tag{3.4}$$

https://doi.org/10.1017/jfm.2012.433 Published online by Cambridge University Press

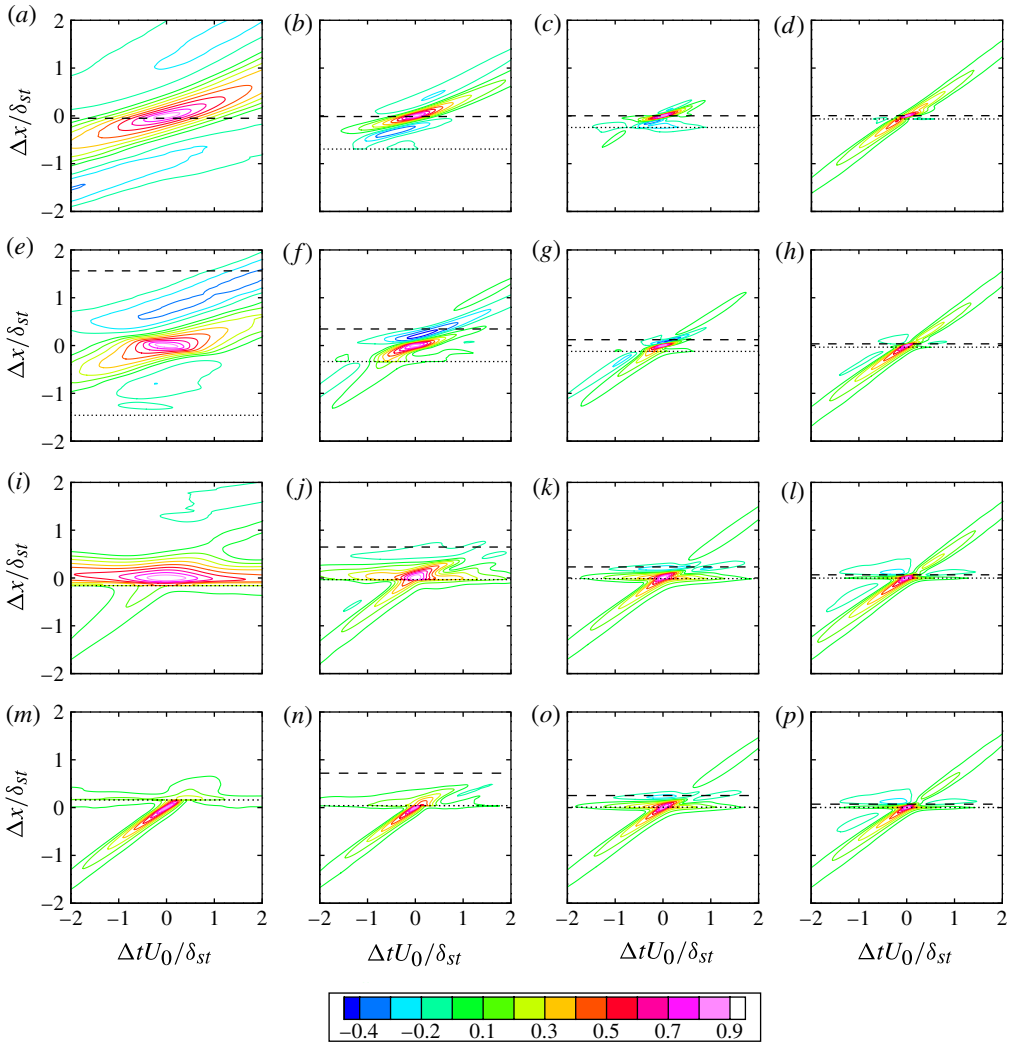


FIGURE 12. Space–time correlation coefficient $C_{pp}(\Delta x, \Delta t; x)$ for backward-facing steps at four streamwise locations. From left: first column, B01; second column, B04; third column, B16; fourth column, B64. From top: first row, $x \simeq x_r$; second row, $x \simeq 0.5x_r$; third row, $x \simeq 0.05x_r$; fourth row, $x \simeq -0.3h$. Dotted and dashed horizontal lines denote locations of step and mean reattachment, respectively.

where Re(·) and Im(·) are the real and imaginary parts of a complex number, respectively.

Figure 12 shows the correlation coefficient $C_{pp}(\Delta x, \Delta t; x)$ for backward steps at four streamwise positions. It is plotted on the boundary-layer scale (δ_{st}) to illustrate the varying extent to which steps of different heights affect the boundary-layer structures. Dotted and dashed horizontal lines represent the locations of step vertical face and mean reattachment, respectively. Columns and rows in the figure are arranged by different step heights and streamwise locations, respectively. As the step height decreases (moving from left to right columns), the shape of the contours becomes more similar to that from an equilibrium boundary layer shown in figure 11, indicating

https://doi.org/10.1017/jfm.2012.433 Published online by Cambridge University Press

diminishing effects of the step-generated flow structures and increasing effects of the boundary-layer eddies on the unsteady surface pressure. Near the step lower corner inside of the separation bubble ($x \simeq 0.05x_r$; second row from the bottom), the nearly horizontal contour lines for B01 indicate that the pressure fluctuations are mainly associated with nearly stationary eddies. In the middle of the recirculation bubble ($x \simeq 0.5x_r$) of all steps except B64, two slanted lobes of similar shape but of opposite sign are seen. Their slopes are smaller than that of the lobes in figure 11 and thus the related pressure sources convect more slowly than the boundary-layer sources. It will be shown in § 4 that these structures are caused by vortical structures generated in the separated shear layer. The surface pressure fluctuations in the reattachment region ($x \simeq x_r$) continue to be dominated by the convecting shear-layer-generated structures.

Figure 13 shows $C_{pp}(\Delta x, \Delta t; x)$ for forward steps. As with the backward steps, an increasing influence of the boundary layer on the unsteady surface pressure with decreasing step height is observed. However, forward steps modify the flow more severely than backward steps. At a short distance upstream of the step ($x \simeq -h$), flow is strongly retarded by the step, and slow convection speeds are reflected in the shallow slopes of the lobes formed by contour lines. At $x \simeq h$, which is near the middle of the recirculation bubbles of F01 and F04, vortical structures are identified as in the separated regions of B01, B04 and B16. On the other hand, the shapes of the contours for the two smaller steps F16 and F64 are qualitatively different owing to the absence of a separation bubble. Near the reattachment locations of F01 and F04 ($x \simeq 2.2h$), the pressure fluctuations are dominated by the convecting vortical structures and well correlated across the reattachment line. Farther downstream at $x \simeq 12h$, the structures grow in size and convection velocities increase.

The phase angle $\phi(\Delta x, \omega; x)$ of the cross-spectrum of surface pressure from B01 is shown in figure 14 at two frequencies $fx_r/U_0 \simeq 0.2$ and 0.6. Each curve corresponds to a different reference pressure location x inside of the recirculation bubble. From (3.4), the convection velocity is given by

$$U_c(\Delta x, f; x) = \frac{2\pi f}{\phi/\Delta x}, \tag{3.5}$$

where the denominator is the slope of a line connecting the x intercept $(x, 0)$ and any point $(x + \Delta x, \phi)$ on the curve representing a given reference pressure location x. In the rear part of the recirculation bubble $x/x_r \geqslant 0.7$, the slope of the curves is fairly independent of Δx, and convection velocities are $0.19U_0$ and $0.37U_0$ for $fx_r/U_0 \simeq 0.2$ and 0.6, respectively. As the reference pressure location x is moved closer to the step, the slope of the curves shows complicated changes.

At the frequency $fx_r/U_0 \simeq 0.2$ (figure 14*a*), the phase curve for the reference location $x/x_r = 0.40$ has a minimum value and grows on both sides. It results from pressure-inducing flow structures convecting downstream (positive slope and U_c) for $\Delta x > 0$ and upstream (negative slope and U_c) for $\Delta x < 0$. Negative convection velocities have also been observed by some researchers (Heenan & Morrison 1998; Hudy, Naguib & Humphreys 2003) in the front part of a separation bubble. An examination of similar phase angle plots from other steps indicates that negative convection velocities occur only for F01, B01 and B04. In the front part of the separation bubble, slow- or upstream-moving eddies near the wall dominate the surface pressure fluctuations, while shear-layer-generated vortical structures dominate farther downstream from the step (see figure 12 at locations $x \simeq 0.5x_r$ and $x \simeq x_r$). For the location $x/x_r = 0.26$, the convection velocity is $-0.10U_0$ for $\Delta x \leqslant 0$. For locations $x/x_r \leqslant 0.22$, a phase jump from a negatively sloped line to a positively

https://doi.org/10.1017/jfm.2012.433 Published online by Cambridge University Press

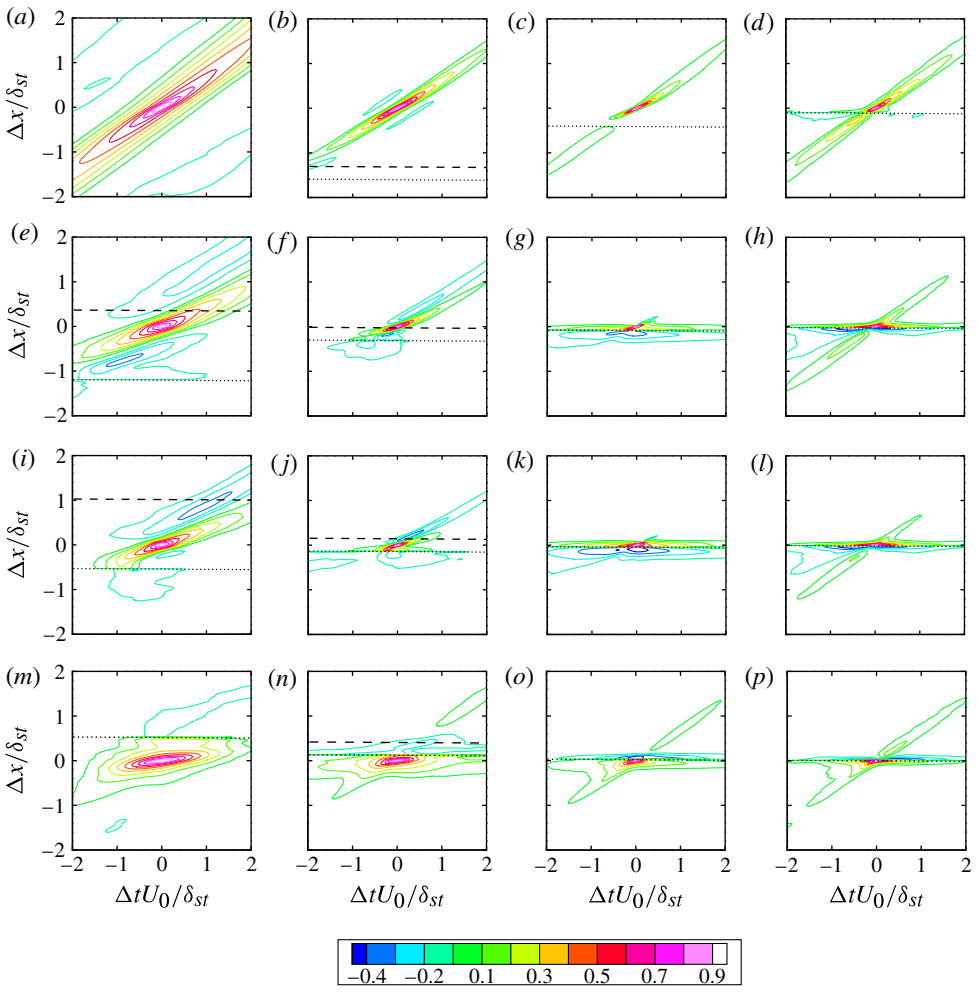


FIGURE 13. Space–time correlation coefficient $C_{pp}(\Delta x, \Delta t; x)$ for forward-facing steps at four streamwise locations. From left: first column, F01; second column, F04; third column, F16; fourth column, F64. From top: first row, $x \simeq 12h$; second row, $x \simeq 2.2h$; third row, $x \simeq h$; fourth row, $x \simeq -h$. Dotted and dashed horizontal lines denote locations of step and reattachment, respectively.

sloped line is observed; see, for example, the curve for $x/x_r = 0.053$, where a downward jump occurs at $0.3 \lesssim (x + \Delta x)/x_r \lesssim 0.4$. The phase curves at many different x locations in the near-step region reveal that the negatively sloped line does not change much, but the positively sloped line jumps downward or upward, with a difference of exactly 2π between the downward- and upward-jump cases. Recently, Hudy *et al.* (2003) experimentally observed a very similar jump in their phase curve for flow over a fence. They hypothesized that it may be associated with the absolute instability of the recirculation bubble at the shear-layer flapping frequency $fx_r/U_0 \simeq 0.15$. However, the lack of flapping-frequency peak in our data precludes making such a connection. At the frequency $fx_r/U_0 \simeq 0.6$ (figure 14*b*), the phase curves behave much more regularly and negative convection velocities are rare,

https://doi.org/10.1017/jfm.2012.433 Published online by Cambridge University Press

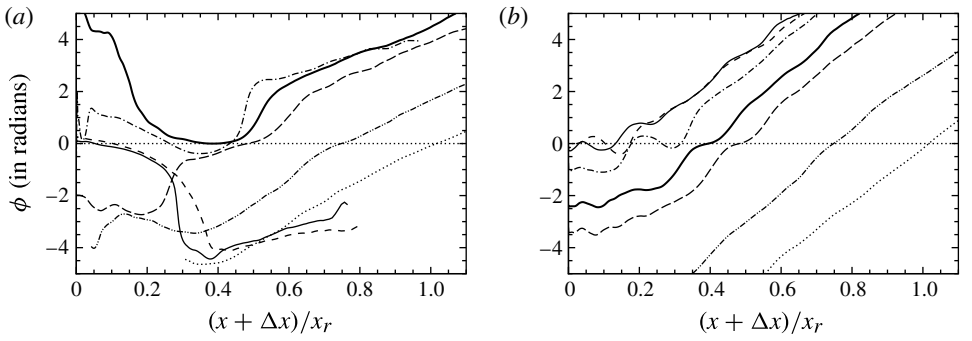


FIGURE 14. Phase angle $\phi(\Delta x, \omega; x)$ defined in (3.4) for B01 at frequencies (*a*) $fx_r/U_0 \simeq 0.20$ and (*b*) $fx_r/U_0 \simeq 0.60$. Curves: ——, $x/x_r \simeq 0.053$; – – –, $x/x_r \simeq 0.10$; —·—, $x/x_r \simeq 0.26$; ——, $x/x_r \simeq 0.40$; — —, $x/x_r \simeq 0.48$; —··—, $x/x_r \simeq 0.75$; ·····, $x/x_r \simeq 1.0$.

indicating that the negative convection velocity is mainly related to low-frequency motions.

4. Pressure–velocity correlations

Further insight into the production mechanisms for surface pressure and their dependence on step height can be gained from the space–time correlations between surface pressure and velocity fluctuations. The cross-correlation between surface pressure fluctuations at $\boldsymbol{x}$ and streamwise velocity fluctuations at $\boldsymbol{x} + \Delta\boldsymbol{x}$ with a time difference Δt is defined as

$$R_{pu}(\Delta\boldsymbol{x}, \Delta t; \boldsymbol{x}) = \langle p'(\boldsymbol{x}, t) u'(\boldsymbol{x} + \Delta\boldsymbol{x}, t + \Delta t) \rangle. \tag{4.1}$$

The corresponding correlation coefficient is

$$C_{pu}(\Delta\boldsymbol{x}, \Delta t; \boldsymbol{x}) = \frac{R_{pu}(\Delta\boldsymbol{x}, \Delta t; \boldsymbol{x})}{R_{pp}(0, 0; \boldsymbol{x})^{1/2} R_{uu}(0, 0; \boldsymbol{x} + \Delta\boldsymbol{x})^{1/2}}. \tag{4.2}$$

Values R_{pv} and C_{pv} for the cross-stream velocity fluctuations are obtained analogously. In the following analyses, the correlation coefficients in the x–y plane ($\Delta z = 0$) are examined. Time series of flow velocities in four x–y planes evenly spaced over the spanwise domain were used to compute the correlations for B(F)04, B(F)16 and B(F)64, and the results are averaged over these four planes, which are statistically equivalent.

The correlation-coefficient fields from backward steps B04, B16 and B64 are presented in figure 15 for the surface pressure at the maximum p_{rms} location. On the boundary-layer scale (figure 15*a*), the smallest step B64 is hardly visible, and its C_{pu} and C_{pv} distributions resemble those in the upstream equilibrium boundary layer. Close-up views of the correlations near the steps can be found in figure 15(*b*), which is plotted on the h scale. Flows over the larger steps B04 and B16 exhibit similar-looking correlated regions downstream of the step. They are evidence of coherent vortical structures generated by the separated shear layer. These observations corroborate the conclusions drawn previously that the dominant mechanism for surface pressure fluctuations is the vortical structures in the separated shear layer in the case of larger backward steps, whereas it is the turbulent fluctuations in the boundary layer

https://doi.org/10.1017/jfm.2012.433 Published online by Cambridge University Press

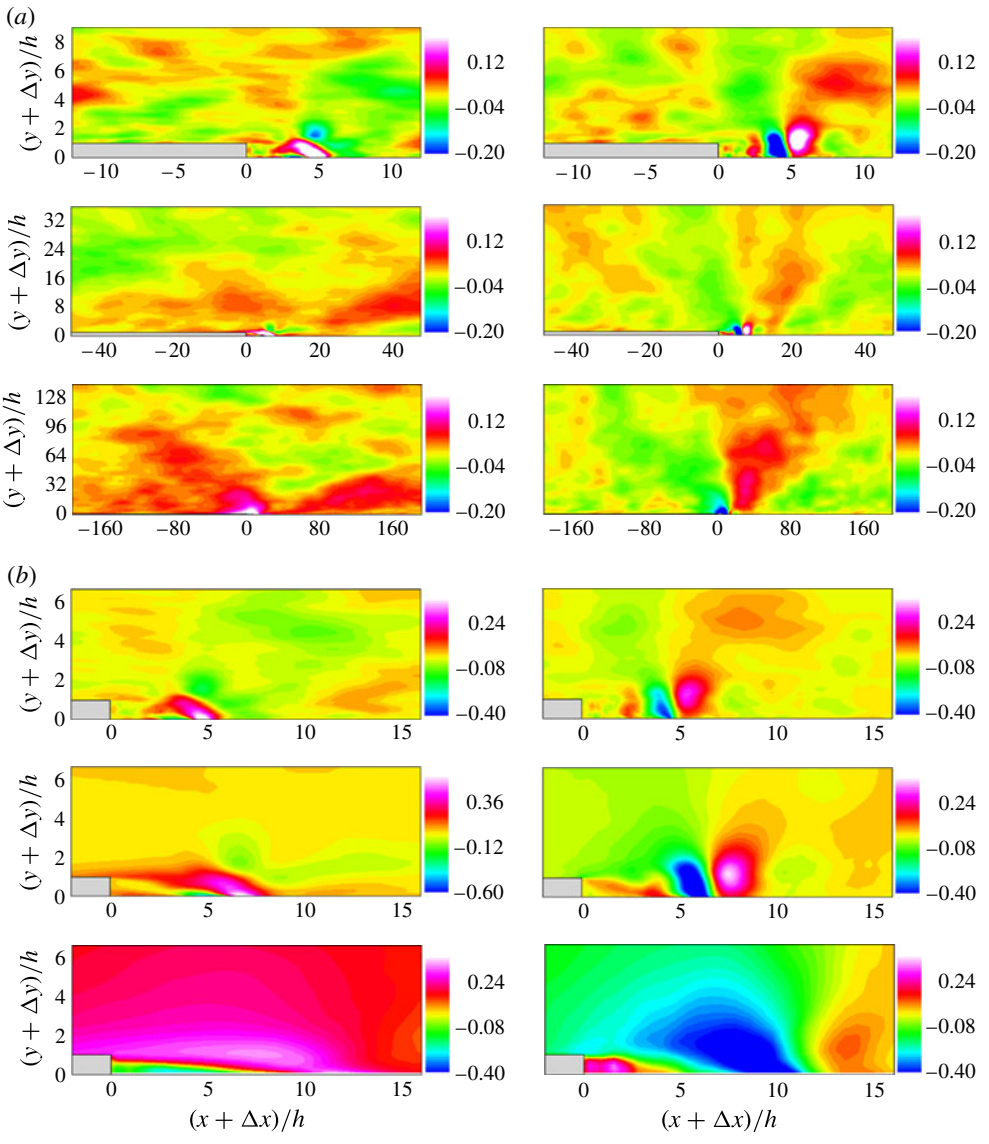


FIGURE 15. Correlation coefficients $C_{pu}(\Delta \boldsymbol{x}, 0; \boldsymbol{x})$ (left column) and $C_{pv}(\Delta \boldsymbol{x}, 0; \boldsymbol{x})$ (right column) for backward steps: (*a*) larger region up to $y/\delta_{st} \simeq 1$; and (*b*) region near the step. B04, B16 and B64 are shown in the top, middle and bottom rows, respectively, for both panels. The reference pressure is measured at the maximum p_{rms} location: $x/h = 4.6$, 6.5 and 11.2 for B04, B16 and B64, respectively.

for the smallest backward step. Although not shown here, the correlation-coefficient fields from the forward steps show similar dependence on step height.

Kiya & Sasaki (1983), in their study of flow over a blunt flat plate, suggested visualizing the shear-layer-generated vortical structures in an 'averaged' sense by considering a vector field whose x and y components are C_{pu} and C_{pv}, respectively. This is illustrated in figure 16 for the cases of B04 and F04. The centre of the vortical structure is the intersection of the loci of $C_{pu} = 0$ and $C_{pv} = 0$, and the major axis of

https://doi.org/10.1017/jfm.2012.433 Published online by Cambridge University Press

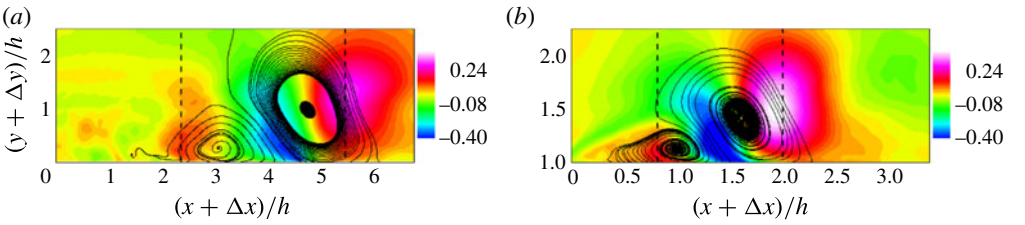


FIGURE 16. Streamlines of the vector field (C_{pu}, C_{pv}) and C_{pv} contours for (*a*) B04 and (*b*) F04. The reference pressure is measured at the maximum p_{rms} location and $\Delta t = 0$. The two vertical dashed lines are separated by a distance of $0.6x_r$ (B04) and $0.55x_r$ (F04), and indicate the size of the vortical structures.

the vortex, defined as the bisector of the two lines $C_{pu} = 0$ and $C_{pv} = 0$, is seen to incline by an angle of 48 and 51° to the negative x axis for B04 and F04, respectively. These are comparable to the 45° obtained by Kiya & Sasaki (1983). The size of the vortical structures, measured in figure 16 as the distance between two neighbouring positive peaks of C_{pv}, is 60 and 55 % of x_r for B04 and F04, respectively, and confirms that the shear-layer-generated flow structures scale with x_r.

The C_{pv} fields with $\Delta t = 0$ in figure 17 demonstrate how the pressure fluctuations at various streamwise locations are affected by different flow regions for the cases of B04 and F04. A short distance downstream of B04 at $x/x_r = 0.1$, significant correlation of the velocity fluctuations above the step with the surface pressure indicates a significant contribution of the boundary layer. Moreover, the region near the step lower corner is seen to contribute to some extent. At $x/x_r = 0.3$, the vortical structure in the shear layer is already recognizable, although a somewhat strong influence of the boundary layer still exists. As the surface pressure location is moved farther downstream, the boundary-layer contribution gradually diminishes and the shear layer becomes more important. Downstream of the reattachment at $x/x_r = 1.5$, the surface pressure is mainly caused by the downstream-convecting vortices resulting from the shear layer. Upstream of F04 at $x/h = -2$ and -0.8, velocity fluctuations upstream of the step and near the step upper corner are the dominant source for the surface pressure fluctuations. Downstream of the step, formation and convection of vortices are again observed; their contribution to the surface pressure increases as the pressure location is moved farther downstream.

Figure 18 presents the C_{pv} fields with different Δt values for the flow over B04. The time difference between two consecutive rows is $\Delta t U_0/h = 3.83$. The sequence of plots clearly identifies convecting flow structures that cause surface pressure fluctuations at two given locations. At $x/x_r = 0.3$ (figure 18*a*), the surface pressure is correlated with the upstream boundary-layer flow at negative Δt values and with the shear-layer vortical structures at positive Δt values. On the other hand, the surface pressure at $x/x_r = 0.88$ (figure 18*b*) is less correlated with the boundary-layer velocity fluctuations. Convection speeds of the pressure-inducing flow structures can be estimated from the figure, since their travel distance and time are known. At the pressure location $x/x_r = 0.3$, the packet of correlated boundary-layer fluctuations with its maximum at $y/h = 2.2$ convects at $0.7U_0$, whereas the shear-layer-generated structures convect at $0.3U_0$. For the pressure location $x/x_r = 0.88$, boundary-layer structures move at $0.82U_0$, while the shear-layer structures move at $0.33U_0$. Figure 19 shows the C_{pv} fields with different Δt values for the flow over F04 at streamwise locations $x/x_r = 0.3$ (figure 19*a*) and 0.74 (figure 19*b*). The former sees

https://doi.org/10.1017/jfm.2012.433 Published online by Cambridge University Press

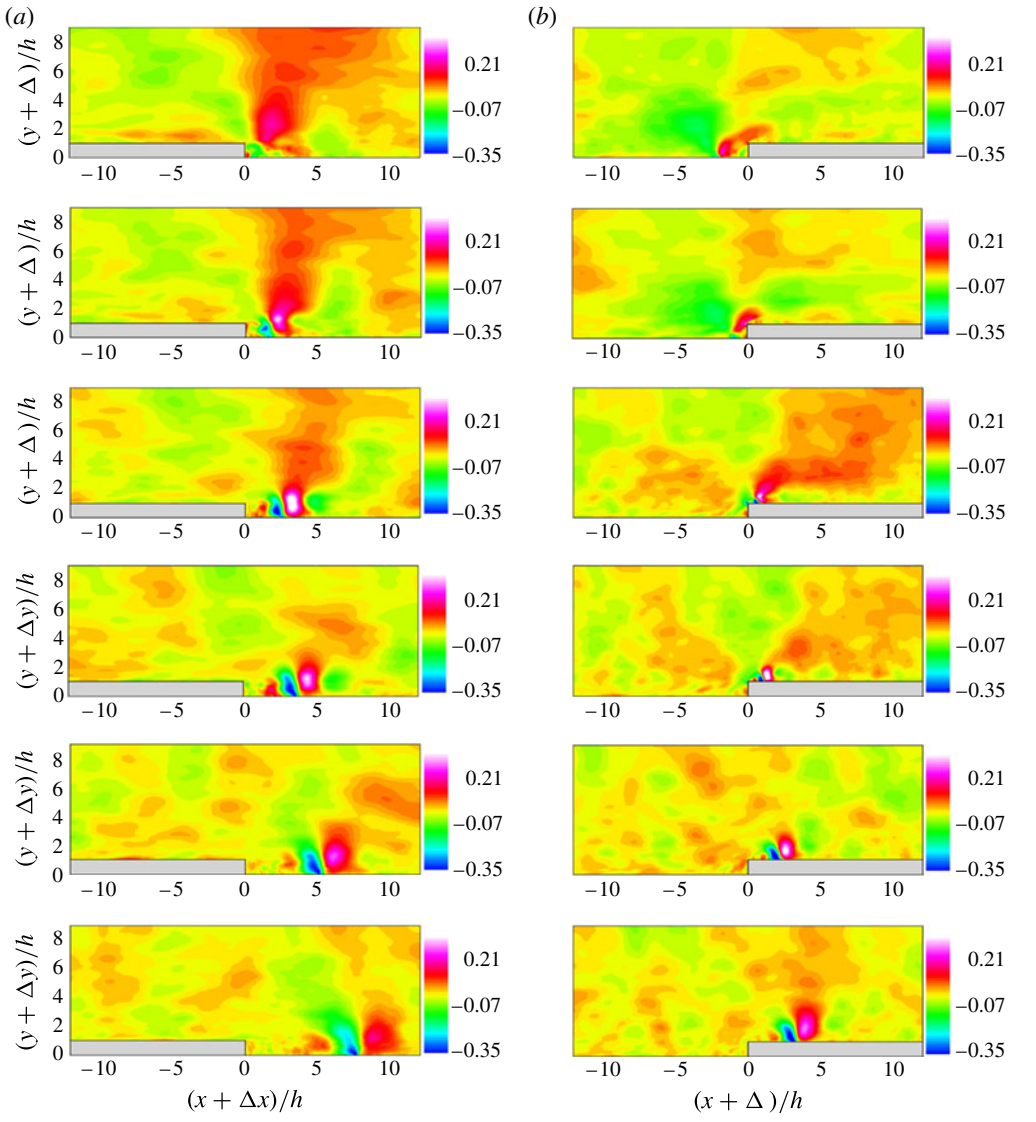


FIGURE 17. Surface pressure–velocity correlation coefficients $C_{pv}(\Delta\boldsymbol{x}, 0; \boldsymbol{x})$ for (*a*) B04 and (*b*) F04 at different streamwise locations $\boldsymbol{x}$. For B04, the reference pressure is measured, from top to bottom, at $x/x_r = 0.1$, 0.3, 0.5, 0.7, 1.0 and 1.5. For F04, the reference pressure is measured, from top to bottom, at $x/h = -2$, -0.8, $x/x_r = 0.3$, 0.5, 1.0 and 1.5.

more pronounced effects of the boundary-layer velocity fluctuations, while the latter is dominated by the shear-layer-induced structures. The convection velocities of the shear-layer vortical structures are $0.25U_0$ and $0.35U_0$ for pressure locations $x/x_r = 0.3$ and $x/x_r = 0.74$, respectively.

For both B04 and F04 cases as well as other steps with coherent shear-layer vortices, the convection speed for the shear-layer vortical structures is much slower than that for the boundary-layer structures. This is expected because the boundary-layer structures are farther away from the wall, where the mean velocity is larger. Furthermore, the

https://doi.org/10.1017/jfm.2012.433 Published online by Cambridge University Press

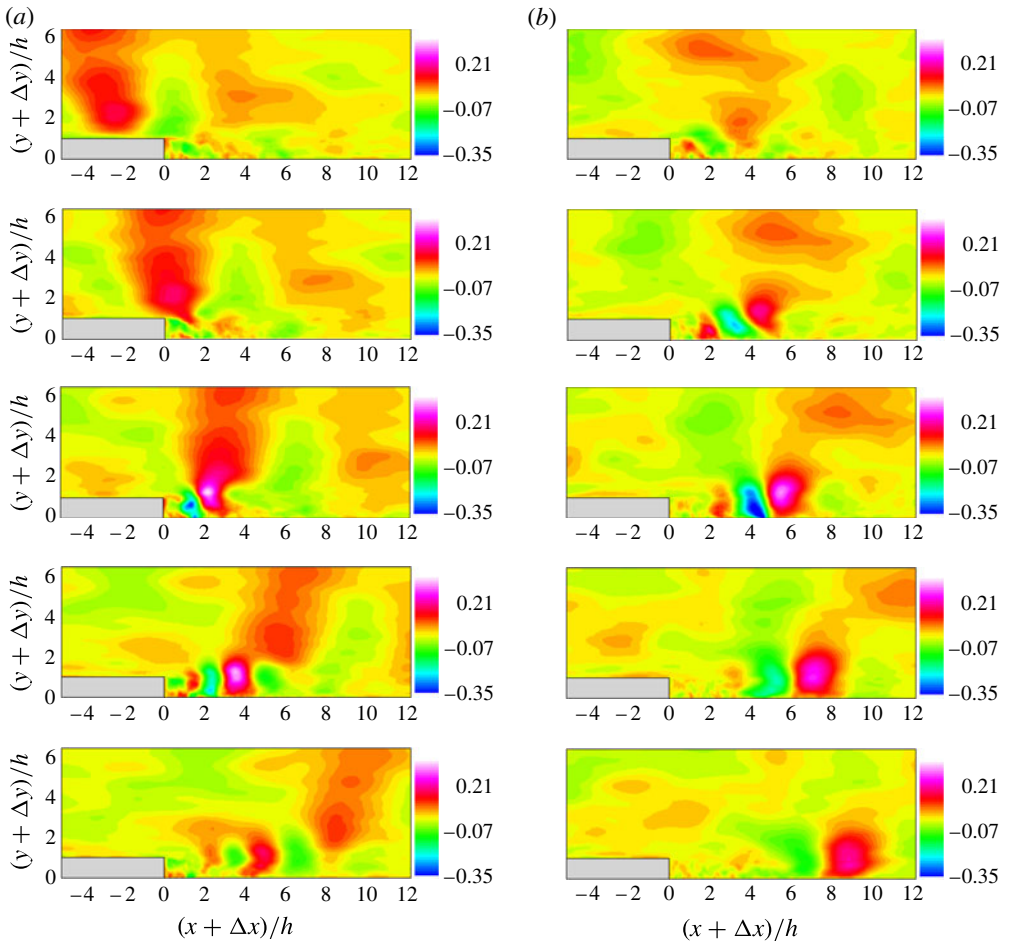


FIGURE 18. Surface pressure–velocity correlation coefficients $C_{pv}(\Delta\boldsymbol{x}, \Delta t; \boldsymbol{x})$ for B04 with different time separations Δt. The reference pressure is measured at (*a*) $x/x_r = 0.3$ and (*b*) $x/x_r = 0.88$. From top to bottom, the temporal separation $\Delta t U_0/h$ is −7.66, −3.83, 0, 3.83 and 7.66.

speed of the shear-layer structures is determined by the high-speed and low-speed flows separated by the shear layer, and the low-speed flow in the separation bubble retards the motion of these structures. If the convection speed of the vortical structures related to the surface pressure at the maximum p_{rms} location (figures 18*b* and 19*b*) is considered in connection with the 'vortex-shedding' frequency, then $fx_r/U_0 \simeq 0.6$ (see figure 9) and $U_c/U_0 \simeq 0.34$ give $l/x_r \simeq 0.57$ (where l is the size of vortical structures), which is close to that obtained earlier from figure 16.

5. Boundary-layer recovery downstream of steps

The high level of pressure fluctuations induced by steps decreases as the perturbed flow relaxes downstream of the step towards an equilibrium boundary layer. The distance associated with this recovery process is of practical importance and is discussed in this section. First, integral boundary-layer quantities such as the

https://doi.org/10.1017/jfm.2012.433 Published online by Cambridge University Press

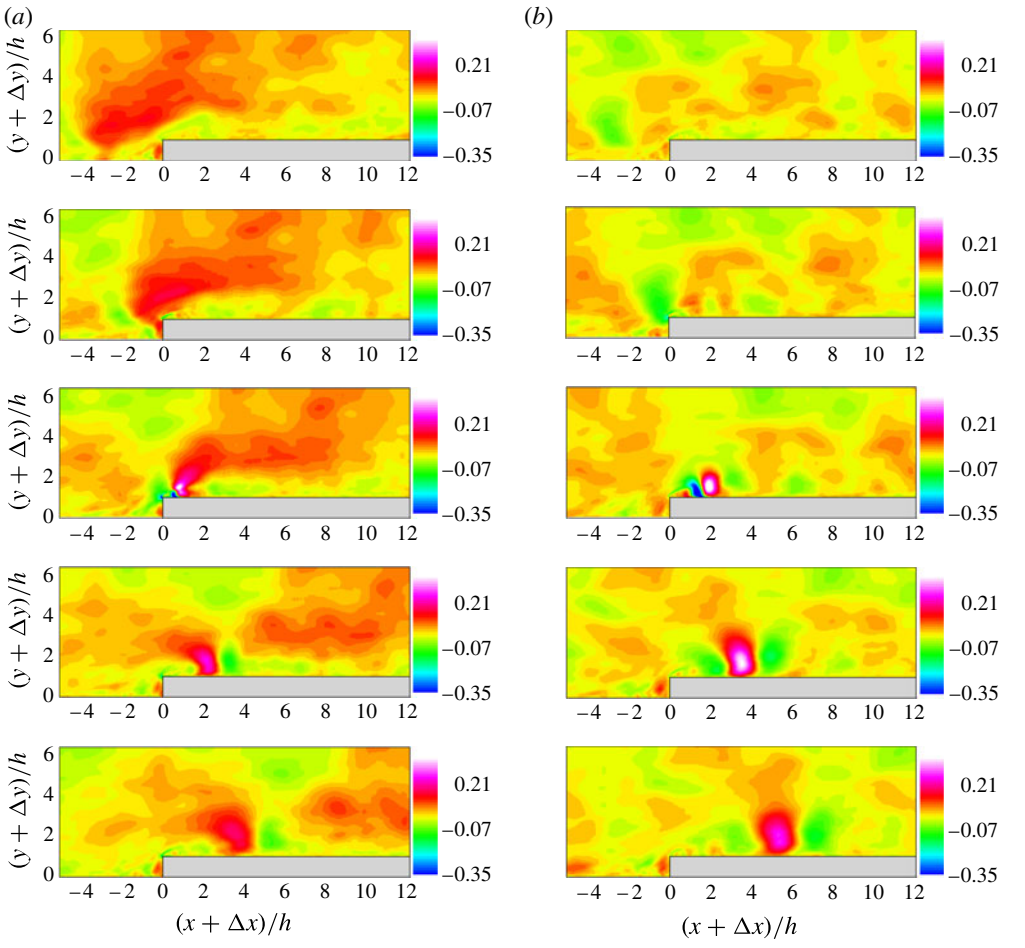


FIGURE 19. Surface pressure–velocity correlation coefficients $C_{pv}(\Delta \boldsymbol{x}, \Delta t; \boldsymbol{x})$ for F04 with different time separations Δt. The reference pressure is measured at (*a*) $x/x_r = 0.3$ and (*b*) $x/x_r = 0.74$. From top to bottom, the temporal separation $\Delta t U_0/h$ is −7.06, −3.53, 0, 3.53 and 7.06.

momentum thickness, the shape factor and the Clauser parameter are considered to characterize the recovery in terms of mean-flow statistics. Then, r.m.s. pressure fluctuations and pressure frequency spectra are examined.

5.1. *Integral boundary-layer quantities*

Shown in figure 20 is the streamwise variation of the boundary-layer momentum thickness θ. Dotted lines depict the streamwise growth of θ for a flat-plate boundary layer and serve as a reference. For the backward steps (solid lines), the boundary layer becomes thinner as the flow approaches the step under the influence of a favourable pressure gradient, and then thickens considerably downstream of the step. For the forward steps (dashed lines), the adverse mean pressure gradient upstream of the step thickens the incoming boundary layer. Downstream of the forward step, both velocity defect and velocity overshoot play a role in determining θ. The former results from flow separation and the latter from flow acceleration over the step. In the case of

https://doi.org/10.1017/jfm.2012.433 Published online by Cambridge University Press

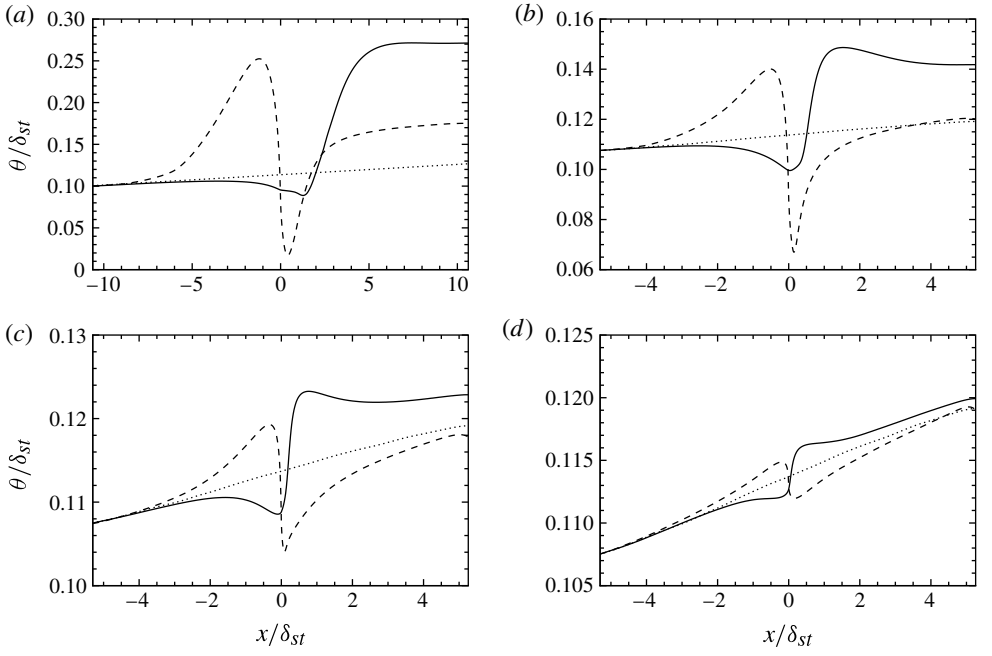


FIGURE 20. Streamwise variation of momentum thickness for (*a*) B(F)01, (*b*) B(F)04, (*c*) B(F)16 and (*d*) B(F)64. Curves: ——, backward-facing step; – – –, forward-facing step; · · · · · ·, unperturbed flat-plate boundary layer from a separate simulation with the same turbulent inflow.

F01, the velocity defect dominates and θ increases above the flat-plate value and remains higher to the end of the computational domain. Note that the momentum thickness is not formally defined in separated regions, and here the same definition as for an attached boundary layer is used to illustrate the deviation from an equilibrium boundary layer. For each step height, the backward step exhibits greater departure of θ downstream from that of a flat-plate boundary layer than the forward step.

The momentum thickness alone does not indicate whether a flow has returned to an equilibrium boundary layer, since the newly established equilibrium boundary layer may have a different thickness. However, an interesting inference can be made when it is considered together with other quantities. Figure 21 shows the streamwise variation of the shape factor $H = \delta^*/\theta$ and the Clauser parameter G downstream of steps. The Clauser parameter is defined as

$$G = \frac{H-1}{H}\sqrt{\frac{2}{C_f}}. \tag{5.1}$$

Values of $H = 1.35$ and $G = 7.3$ obtained far upstream of the smallest steps are plotted as dotted lines. Note that the G value from the LES is slightly larger than 6.8 for an equilibrium zero-pressure-gradient boundary layer (Bradshaw & Wong 1972). The shape factor changes monotonically whereas the Clauser parameter does not for all steps. For B16, F04 and F16, G increases after reaching a minimum. This is consistent with the observations of Bradshaw & Wong (1972) and reflects the behaviour of the skin friction coefficient C_f, which changes non-monotonically downstream of the

https://doi.org/10.1017/jfm.2012.433 Published online by Cambridge University Press

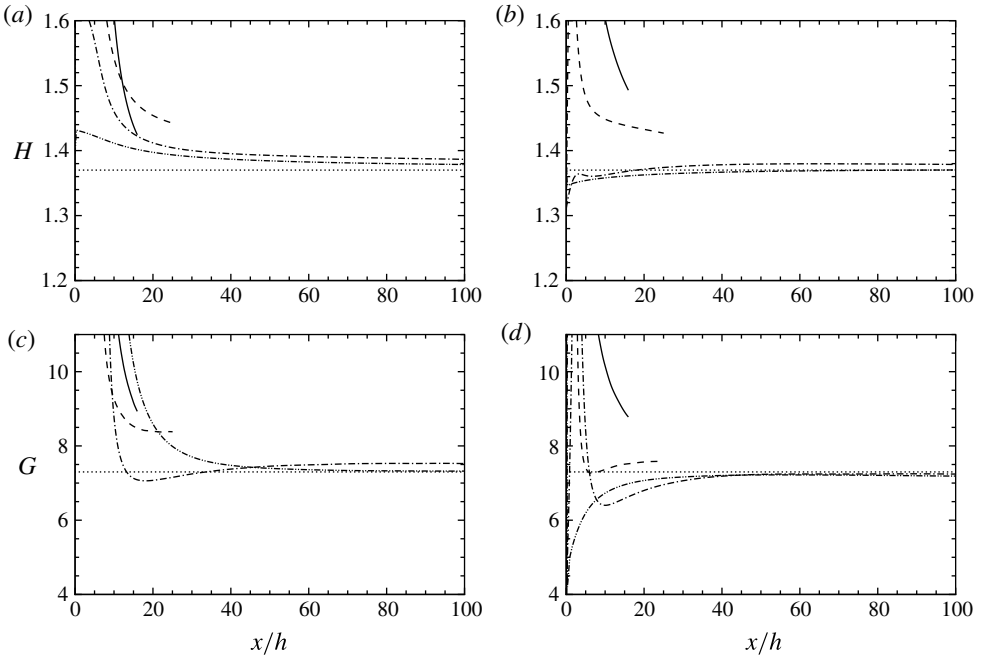


FIGURE 21. Streamwise variations of shape factor H and Clauser parameter G downstream of (a,c) backward steps and (b,d) forward steps. Curves: ——, B(F)01; – – –, B(F)04; — · —, B(F)16; — ·· —, B(F)64; · · · · · ·, far-upstream equilibrium boundary layer.

reattachment location. Both the shape factor and the Clauser parameter indicate that flows over the two smaller steps have returned to an equilibrium boundary layer by the approximate locations $x/h \simeq 80$ (B16), $x/h \simeq 60$ (B64) and $x/h \simeq 50$ (F16 and F64). Flows over the two larger steps B(F)01 and B(F)04 are far from equilibrium at the farthest downstream location. Although not shown here, profiles of mean velocities and Reynolds stresses provide further evidences of these larger steps' non-equilibrium state far downstream of the step. The value of $U^+ = U/u_\tau$ ($u_\tau = \sqrt{\tau_w/\rho}$ is the friction velocity) falls below the universal log-law curve and the large Reynolds stresses in the separated shear layer (see figure 3) are still visible.

The shape factor and the Clauser parameter in figure 21 indicate that flows over the steps B(F)16 and B(F)64 fully recover within the computational domain. Therefore, according to figure 20, the momentum thicknesses of the fully recovered flows downstream of F16 and F64 are close to that of the boundary layer that would be found if the far-upstream flow had not been perturbed and allowed to spatially grow over the same distance. Momentum thicknesses downstream of B16 and B64 are larger than the unperturbed flat-plate value, indicating that the perturbed flows relax into even higher-Reynolds-number boundary layers.

5.2. *Recovery of pressure fluctuations*

Figure 22 shows the decay of r.m.s. pressure fluctuations downstream of the maximum p_{rms} location for all steps except F16 and F64, which do not have a separation bubble. The maximum p_{rms} of each step is used to scale the pressure, and the streamwise distance is scaled with the step height and the mean reattachment length. The location of maximum p_{rms} is ahead of the reattachment point for all steps except

https://doi.org/10.1017/jfm.2012.433 Published online by Cambridge University Press

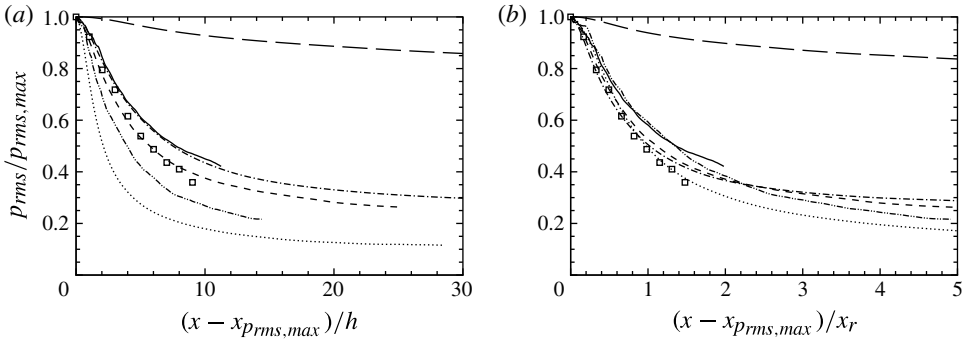


FIGURE 22. Change in p_{rms} (as a fraction of maximum p_{rms}) downstream of the maximum p_{rms} location. Distance is scaled with (*a*) step height and (*b*) mean reattachment length. Curves: ——, B01; – – –, B04; — · —, B16; — —, B64; — ·· —, F01; · · · · · ·, F04; □, Chun *et al.* (2004) for a backward step of $h/\delta = 2.03$.

B64, for which it is behind the reattachment. When the distance is scaled with x_r, the curves from both backward and forward steps collapse better than with h. As in other statistics, the smallest backward step behaves differently, confirming different mechanisms for pressure fluctuations. The reduction in p_{rms} is initially rapid and ∼60 % of the maximum p_{rms} is lost by the time flow moves two reattachment lengths downstream, corresponding to $x/h = 16.4$, 14.7, 21.2, 7.6 and 5.9 for B01, B04, B16, F01 and F04, respectively. The experimental data of Chun *et al.* (2004) show a similar drop, although the comparison may be influenced by Reynolds-number and h/δ differences. The rapid change is due to the decrease in the Reynolds stresses (see figure 5) and the mean velocity gradient in the region. Because of the proximity of the maximum p_{rms} location to the mean reattachment point, it may appear that the flow impingement contributes significantly to the unsteady pressure increase. However, the slope of the curves in figure 22 indicates that the most rapid decrease in p_{rms} in fact occurs at the reattachment location, i.e. largest negative slope at $x = x_r$. The flow impingement does increase the surface pressure fluctuations in the case of B64. However, for larger step heights the increase in fluctuating surface pressure is predominantly caused by the unsteadiness in the shear layer, and the reattachment point, despite having a large p_{rms}, is identified with greater reduction in pressure than increase. Farther downstream, the r.m.s. pressure decreases much more gradually and retains 20–30 % of the maximum p_{rms} at $(x - x_{prms,max})/x_r = 5$, or approximately six reattachment lengths behind the step.

In order to estimate the pressure-recovery distance, the normalized quantity $(p_{rms} - p_{rms,EQ})/p_{rms,EQ}$ is plotted in figure 23 as a function of downstream distance on a logarithmic scale. The surface pressure from all steps should return to a similar p_{rms} value when an equilibrium boundary layer is re-established far downstream of the step. It was previously shown that flows over larger steps recover to a higher-Reynolds-number boundary layer. However, the change in p_{rms} due to the Reynolds-number effect should be small compared to the increase caused by steps. Therefore, the LES value of $p_{rms,EQ}/(\rho U_0^2/2) = 0.0063$ obtained far upstream of smallest steps is used for all steps in the figure. When $(x - x_{prms,max})/x_r \gtrsim 2$, the pressure fluctuations from all steps decay at a similar rate. The slope of -1 indicates that the deviation of p_{rms} from the equilibrium value decays as $1/x$. If the ordinate value of 0.1 ($p_{rms} = 1.1\,p_{rms,EQ}$) is considered the threshold for defining a recovery, an extrapolation of all curves at the

https://doi.org/10.1017/jfm.2012.433 Published online by Cambridge University Press

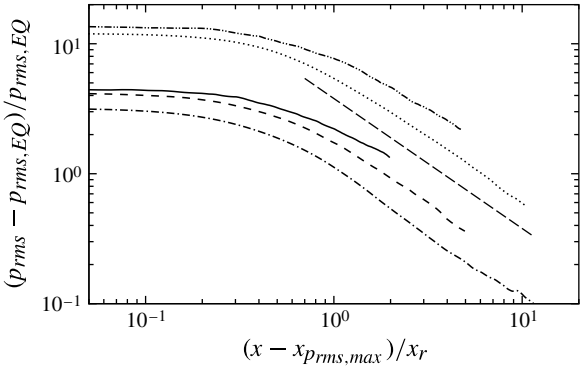


FIGURE 23. Change in p_{rms} downstream of the maximum p_{rms} location. Distance is scaled with the mean reattachment length. Logarithmic scales are used. Curves: ——, B01; – – –, B04; — · —, B16; — ·· —, F01; · · · · · ·, F04; — —, line with slope x^{-1}.

slope of -1 yields approximate $(x - x_{prms,max})/x_r$ values of 30, 20 and 10 for B01, B04 and B16, and 100 and 65 for F01 and F04, respectively. When converted to distances starting from the step and in terms of the step height, they are $x/h = 175$, 107 and 80 for the backward steps, and 295 and 142 for the forward steps. Two important factors in determining the pressure-recovery distance are the peak p_{rms} magnitude and the mean reattachment length x_r. For the former, forward steps are at a disadvantage (i.e. longer recovery distance) due to larger peak p_{rms} values; while for the latter, backward steps are at a disadvantage due to larger x_r. It was shown in § 3.4 that the peak p_{rms} value tends to approach a limiting value with increasing step height. Therefore, the pressure-recovery distances estimated here, especially those of B01 and F01, may apply to many other flows with larger step heights.

Awasthi *et al.* (2011) experimentally found that, for their second largest forward step, the recovery of pressure fluctuations was not complete even at $x/h = 150$. In terms of h/δ, their step corresponds to F04 of the present study, which was shown above to recover in 142 step heights. However, because their $Re_\theta = 15\,500$ is much larger than that in the present study, their step corresponds to F01 in terms of Re_h (26 600 versus 25 920). With the recovery distance of 295 step heights for F01, the current results are in line with the experimental findings. The step Reynolds number Re_h is a more important parameter than h/δ in determining the recovery distance (measured in h) since it dictates the generation and dissipation of large-scale vortical structures that give rise to the non-equilibrium pressure behaviour.

Figure 24 shows the pressure spectra at several locations downstream of all backward steps. For the two smaller steps B16 and B64, the spectra at $x/h = 40$ and $x/h = 100$ are very similar, indicating that the pressure-recovery process is complete. As mentioned earlier, discrepancies in the high-frequency part of the spectrum are largely due to the non-uniform streamwise grid spacings. This explains the smaller high-frequency discrepancies observed for B01 and B64 compared to the two intermediate step heights; the spectra plotted are at locations outside of the mesh stretching region for B01 and at the beginning of the mesh stretching region for B64, where the mesh spacing differences are small, whereas for the two intermediate cases the spectral locations span a major part of the mesh stretching region (from $x/\delta_{st} = 0.3$ to 2.5) with large mesh spacing differences. The boundary-layer recovery should therefore be judged based on the spectra at low to intermediate frequencies.

https://doi.org/10.1017/jfm.2012.433 Published online by Cambridge University Press

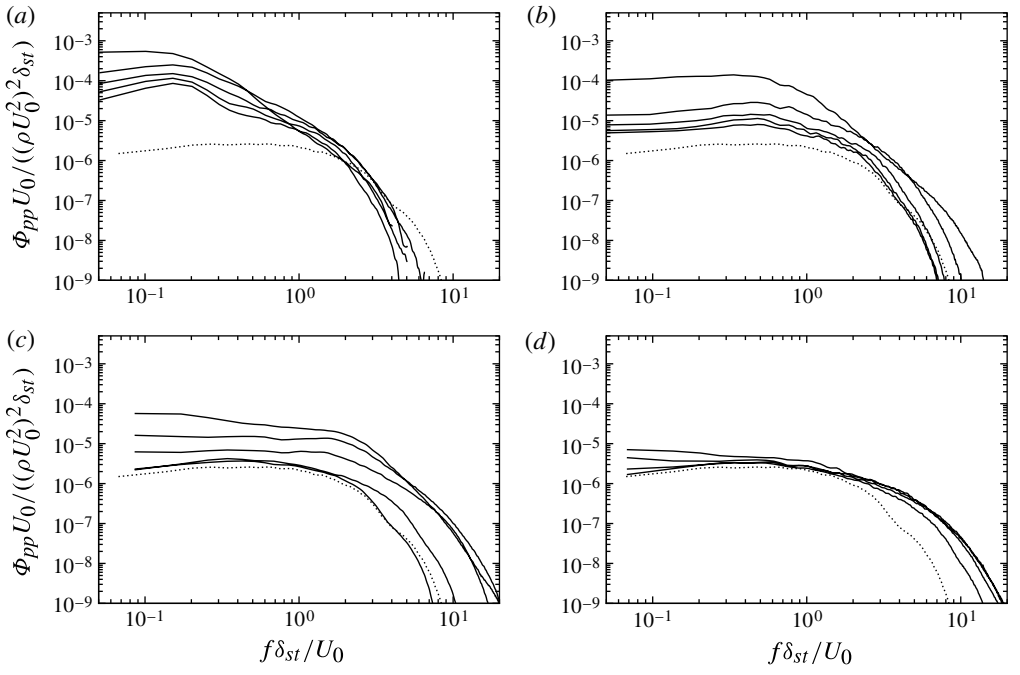


FIGURE 24. Frequency spectra of surface pressure fluctuations downstream of backward steps. The solid lines, in decreasing order of spectral level, are: (*a*) B01, $x/h = 5$, 7.5, 10, 12.5, 16; (*b*) B04, $x/h = 5$, 10, 15, 20, 25; (*c*) B16, $x/h = 7.5$, 10, 15, 40, 100; and (*d*) B64, $x/h = 11$, 24, 40, 100. The dotted line is the far-upstream equilibrium boundary layer.

For B04, the low- to mid-frequency energy level of the spectrum at the last station, $x/h = 25$, is higher than that of equilibrium boundary layer although the shape of the spectrum is similar. For the largest step B01, not only the spectral level but also the shapes are significantly different at the last station $x/h = 16$. The pressure spectra downstream of all forward steps are shown in figure 25. For the two smallest steps F16 and F64, the pressure spectra completely recover. As with B04, the spectral shape for F04 at the last station is similar to that of the equilibrium boundary layer, but the spectral level is higher. For the largest step F01, both spectral level and distribution deviate considerably from the boundary-layer spectrum. The fact that the pressure spectra for B(F)01 and B(F)04 do not recover equilibrium boundary-layer values is consistent with the predictions based on figure 23, since the computational domains are too small.

6. Summary and conclusions

Surface pressure fluctuations induced by a turbulent boundary-layer flow at $Re_\theta = 4755$ over small backward- and forward-facing steps were studied with LES. Four step heights that are 53, 13, 3.3 and 0.83 % of the boundary-layer thickness were considered to elucidate the effect of step height on the unsteady pressure characteristics and source mechanisms. Turbulent velocity fluctuations in both the boundary layer and the separated shear layer are sources of surface pressure fluctuations on all steps, but the extent to which each contributes to the surface pressure varies with the step height. Scaling of various pressure statistics, extensive two-point correlations and their comparison among steps of different heights provided concrete evidence of different mechanisms.

https://doi.org/10.1017/jfm.2012.433 Published online by Cambridge University Press

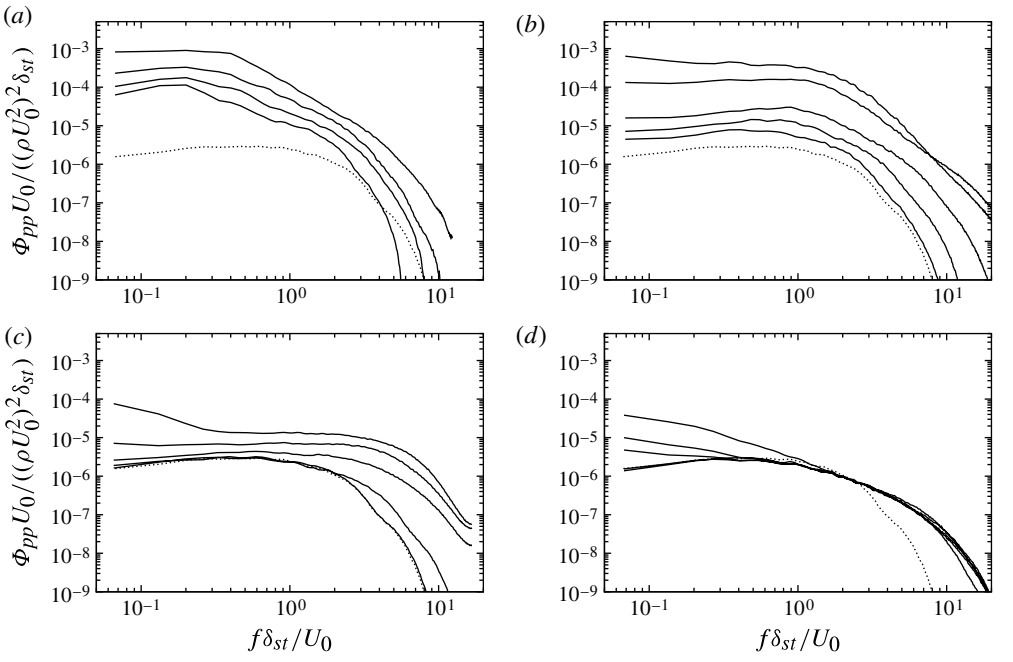


FIGURE 25. Frequency spectra of surface pressure fluctuations downstream of forward steps. The solid lines, in decreasing order of spectral level, are: (*a*) F01, $x/h = 1.7$, 3.4, 10, 16; (*b*) F04, $x/h = 1.5$, 3, 7, 12.5, 25; (*c*) F16, $x/h = 3$, 6, 10, 40, 100; and (*d*) F64, $x/h = 2.2$, 6, 10, 40, 100. The dotted line is the far-upstream equilibrium boundary layer.

For larger steps, vortical structures develop in the separated shear layer and the associated intense turbulent velocity fluctuations are the dominant source. Downstream of slightly less than one reattachment length from the step, the r.m.s. pressure is found to scale with the local maximum cross-stream Reynolds normal stress $\overline{v'^2}_{max}$. At the maximum p_{rms} location, the pressure frequency spectrum consists of an energy-containing range and a higher-frequency range that rolls off at frequencies larger than $fx_r/U_0 \simeq 0.6$. The spectral level of the former is shown to scale with x_r and reflects that the process of energy extraction from mean flow to turbulence occurs on that scale. The roll-off slope of the latter is shown to become shallower with increasing step height and approaches $-7/3$. These observations of the spectrum suggest that an upper bound of $p_{rms}/(\rho U_0^2/2)$ exists for steps of sufficiently large height and are supported by many experiments, which observe approximate values of 0.04 and 0.10 for backward and forward steps, respectively.

As the step height decreases to within the buffer region of the boundary layer, turbulent fluctuations in the boundary layer become the dominant source. With much less intense turbulence in the shear layer, p_{rms} does not scale with $\overline{v'^2}_{max}$ and the roll-off slope of the frequency spectrum becomes steeper, verifying that turbulence–turbulence interaction plays a less important role in producing the surface pressure fluctuations. For the smallest backward step, the maximum p_{rms} is found to occur downstream of the reattachment location; and for the smallest forward step, it occurs upstream of the step vertical face. Despite the absence of mean separation, the second smallest forward step sees some increased level of unsteadiness in the shear layer, and a local maximum p_{rms} is observed downstream of the step.

The downstream recovery of a step-perturbed boundary layer towards an equilibrium boundary layer was investigated in terms of surface pressure fluctuations. For steps

https://doi.org/10.1017/jfm.2012.433 Published online by Cambridge University Press

with a strong separated shear layer, pressure fluctuations are found to decay rapidly for up to three reattachment lengths downstream of the step, within which approximately 60 % of the peak p_{rms} is dissipated. Farther downstream, recovery is much slower and the p_{rms} deviation from the equilibrium value is shown to decay as $1/x$. The recovery distance estimated for the largest backward and forward steps are as large as 175 and 295 step heights, respectively.

Acknowledgements

This work was supported by the Office of Naval Research under grants N00014-09-1-0602 and N00014-12-1-0553 (Program Officer: Dr R. Joslin). Computer time was provided by the US Department of Defense High Performance Computing Modernization Program (HPCMP) through the Naval Research Laboratory Affiliated Resource Center. We wish to thank W. Devenport and S. Glegg for helpful discussions, and J. Hao for assistance with the revision of this paper. Part of this work was presented as AIAA Paper 2010-0006 at the 48th AIAA Aerospace Sciences Meeting, Orlando, Florida, 4–7 January 2010.

REFERENCES

ALVING, A. E. & FERNHOLZ, H. H. 1996 Turbulence measurements around a mild separation bubble and downstream of reattachment. *J. Fluid Mech.* **322**, 297–328.

AWASTHI, M., FOREST, J. B., MORTON, M. A., DEVENPORT, W. & GLEGG, S. A. L. 2011 The disturbance of a high Reynolds number turbulent boundary layer by small forward steps. *AIAA Paper* 2011-2777.

BENDAT, J. S. & PIERSOL, A. G. 2000 *Random Data: Analysis and Measurement Procedures*, 3rd edn. Wiley-Interscience.

BRADSHAW, P. & WONG, F. Y. F. 1972 The reattachment and relaxation of a turbulent shear layer. *J. Fluid Mech.* **52**, 113–135.

BRUNGART, T. A., LAUCHLE, G. C., DEUTSCH, S. & RIGGS, E. T. 2002 Wall pressure fluctuations induced by separated/reattached channel flow. *J. Sound Vib.* **251**, 558–577.

CAMUSSI, R., FELLI, M., PEREIRA, F., ALOISIO, G. & DI MARCO, A. 2008 Statistical properties of wall pressure fluctuations over a forward-facing step. *Phys. Fluids* **20**, 075113.

CAMUSSI, R., GUJ, G. & RAGNI, A. 2006 Wall pressure fluctuations induced by turbulent boundary layers over surface discontinuities. *J. Sound Vib.* **294**, 177–204.

CASTRO, I. P. & EPIK, E. 1998 Boundary layer development after a separated region. *J. Fluid Mech.* **374**, 91–116.

CHUN, S., LIU, Y. Z. & SUNG, H. J. 2004 Wall pressure fluctuations of a turbulent separated and reattaching flow affected by an unsteady wake. *Exp. Fluids* **37**, 531–546.

DANDOIS, J., GARNIER, E. & SAGAUT, P. 2007 Numerical simulation of active separation control by a synthetic jet. *J. Fluid Mech.* **574**, 25–58.

EATON, J. K. & JOHNSTON, J. P. 1981 A review of research on subsonic turbulent flow reattachment. *AIAA J.* **19**, 1093–1100.

EFIMTSOV, B. M., KOZLOV, N. M., KRAVCHENKO, S. V. & ANDERSSON, A. O. 1999 Wall pressure fluctuation spectra at small forward facing steps. *AIAA Paper* 99-1964.

EFIMTSOV, B. M., KOZLOV, N. M., KRAVCHENKO, S. V. & ANDERSSON, A. O. 2000 Wall pressure fluctuation spectra at small backward facing steps. *AIAA Paper* 2000-2053.

FARABEE, T. M. & CASARELLA, M. J. 1984 Effects of surface irregularity on turbulent boundary layer wall pressure fluctuations. *Trans. ASME: J. Vib., Acoust, Stress, Reliab. Design* **106**, 343–350.

FARABEE, T. M. & CASARELLA, M. J. 1986 Measurements of fluctuating wall pressure for separated/reattached boundary layer flows. *Trans. ASME: J. Vib., Acoust, Stress, Reliab. Design* **108**, 301–307.

FRICKE, F. R. 1971 Pressure fluctuations in separated flows. *J. Sound Vib.* **17**, 113–123.

GEORGE, W. K., BEUTHER, P. D. & ARNDT, R. E. A. 1984 Pressure spectra in turbulent free shear flows. *J. Fluid Mech.* **148**, 155–191.

https://doi.org/10.1017/jfm.2012.433 Published online by Cambridge University Press

HEENAN, A. F. & MORRISON, J. F. 1998 Passive control of pressure fluctuations generated by separated flow. *AIAA J.* **36**, 1014–1022.

HUDY, L. M., NAGUIB, A. M. & HUMPHREYS, W. M. 2003 Wall-pressure-array measurements beneath a separating/reattaching flow region. *Phys. Fluids* **15**, 706–717.

JI, M. & WANG, M. 2010 Sound generation by turbulent boundary-layer flow over small steps. *J. Fluid Mech.* **654**, 161–193.

KIYA, M. & SASAKI, K. 1983 Structure of a turbulent separation bubble. *J. Fluid Mech.* **137**, 83–113.

KRAICHNAN, R. H. 1956 Pressure fluctuations in turbulent flow over a flat plate. *J. Acoust. Soc. Am.* **28**, 378–390.

LARGEAU, J. F. & MORINIERE, V. 2007 Wall pressure fluctuations and topology in separated flows over a forward-facing step. *Exp. Fluids* **42**, 21–40.

LAUCHLE, G. C. & KARGUS, W. A. IV 2000 Scaling of turbulent wall pressure fluctuations downstream of a rearward facing step. *J. Acoust. Soc. Am.* **107**, L1–L6.

LECLERCQ, D. J. J., JACOB, M. C., LOUISOT, A. & TALOTTE, C. 2001 Forward–backward facing step pair: aerodynamic flow, wall pressure and acoustic characterization. *AIAA Paper* 2001-2249.

LEE, I. & SUNG, H. J. 2001 Characteristics of wall pressure fluctuations in separated and reattaching flows over a backward-facing step. Part I. Time-mean statistics and cross-spectral analyses. *Exp. Fluids* **30**, 262–272.

LEE, I. & SUNG, H. J. 2002 Multiple-arrayed pressure measurement for investigation of the unsteady flow structure of a reattaching shear layer. *J. Fluid Mech.* **463**, 377–402.

LUND, T. S., WU, X. & SQUIRES, K. D. 1998 Generation of turbulent inflow data for spatially-developing boundary layer simulations. *J. Comput. Phys.* **140**, 233–258.

MABEY, D. G. 1972 Analysis and correlation of data on pressure fluctuations in separated flow. *J. Aircraft* **9**, 642–645.

MABEY, D. G. 1982 Comment on 'A review of research on subsonic turbulent flow attachment'. *AIAA J.* **20**, 1632.

MOHSEN, A. M. 1968 Experimental investigation of the wall pressure fluctuations in subsonic separated flows. *Tech. Rep.* D6-17094. Boeing Company.

MOSS, W. D. & BAKER, S. 1980 Re-circulating flows associated with two-dimensional steps. *Aeronaut. Q.* **31**, 151–172.

NA, Y. & MOIN, P. 1998*a* Direct numerical simulation of a separated turbulent boundary layer. *J. Fluid Mech.* **374**, 379–405.

NA, Y. & MOIN, P. 1998*b* The structure of wall-pressure fluctuations in turbulent boundary layers with adverse pressure gradient and separation. *J. Fluid Mech.* **377**, 347–373.

PANTON, R. L. & LINEBARGER, J. H. 1974 Wall pressure spectra calculations for equilibrium boundary layers. *J. Fluid Mech.* **65**, 261–287.

SIGURDSON, L. W. 1995 The structure and control of a turbulent reattaching flow. *J. Fluid Mech.* **298**, 139–165.

SIMPSON, R. L. 1989 Turbulent boundary-layer separation. *Annu. Rev. Fluid Mech.* **21**, 205–234.

SIMPSON, R. L., CHEW, Y.-T. & SHIVAPRASAD, B. G. 1981 The structure of a separating turbulent boundary layer. Part 1. Mean flow and Reynolds stresses. *J. Fluid Mech.* **113**, 23–51.

SIMPSON, R. L., GHODBANE, M. & MCGRATH, B. E. 1987 Surface pressure fluctuations in a separating turbulent boundary layer. *J. Fluid Mech.* **177**, 167–186.

SONG, S., DEGRAAFF, D. B. & EATON, J. K. 2000 Experimental study of a separating, reattaching, and redeveloping flow over a smoothly contoured ramp. *Intl J. Heat Fluid Flow* **21**, 512–519.

TACHIE, M. F., BALACHANDAR, R. & BERGSTROM, D. J. 2001 Open channel boundary layer relaxation behind a forward facing step at low Reynolds numbers. *Trans. ASME: J. Fluids Engng* **123**, 539–544.

YOU, D., MITTAL, R., WANG, M. & MOIN, P. 2004 Computational methodology for large-eddy simulation of tip-clearance flows. *AIAA J.* **42**, 271–279.

https://doi.org/10.1017/jfm.2012.433 Published online by Cambridge University Press